



Advances in MXene Films: Synthesis, Assembly, and Applications

Xiaohua Li¹ · Feitian Ran¹ · Fan Yang¹ · Jun Long¹ · Lu Shao¹

Received: 16 December 2020 / Revised: 1 January 2021 / Accepted: 19 January 2021 / Published online: 7 March 2021
© The Author(s) 2021

Abstract

A growing family of two-dimensional (2D) transition metal carbides or nitrides, known as MXenes, have received increasing attention because of their unique properties, such as metallic conductivity and good hydrophilicity. The studies on MXenes have been widely pursued, given the composition diversity of the parent MAX phases. This review focuses on MXene films, an important form of MXene-based materials for practical applications. We summarized the synthesis methods of MXenes, focusing on emerging synthesis strategies and reaction mechanisms. The advanced assembly technologies of MXene films, including vacuum-assisted filtration, spin-coating methods, and several other approaches, were then highlighted. Finally, recent progress in the applications of MXene films in electrochemical energy storage, membrane separation, electromagnetic shielding fields, and burgeoning areas, as well as the correlation between compositions, architecture, and performance, was discussed.

Keywords MXene films · Synthesis · Assembly · Mechanism · Applications

Introduction

Since the discovery of mechanically exfoliated graphene in 2004 [1], research on ultrathin two-dimensional (2D) nanomaterials has grown exponentially in the fields of materials, material chemistry, and nanotechnology. Following graphene, a variety of 2D nanomaterials, such as antimonene [2, 3], phosphorene [4], hexagonal boron nitride [5], transition metal disulfides [6], layered metal oxides, and layered double hydroxides, have been reported [7, 8]. These ultrathin 2D materials have unique physical and chemical properties that are different from bulk materials because of the existence of quantum confinement effects [9]. Two-dimensional nanomaterials have shown great application prospect in physics, chemistry, and biology given their compact and ordered structure, and become research hotspot.

Two-dimensional transition metal carbides, or nitrides, known as MXenes, are lamellar structures that are widely

used in many fields, especially in electrochemistry. MXenes are generally fabricated by selective etching the A layers from the corresponding parent MAX phase, which are layered ternary carbides or nitrides and denoted as $M_{n+1}AX_n$ ($n = 1-3$), where M is an early transition metal, A primarily represents IIIA or IVA element, and X is C and/or N [10, 11]. $Ti_3C_2T_x$ is a common representative of MXenes, which is usually yielded through selectively etching the Al layers in Ti_3AlC_2 powders [12, 13]. Exfoliated MXene sheets are usually several atomic layers thick with excellent electrical conductivity, and the surfaces are covered by a mixture of $-OH$, $-O$, and $-F$ terminations [14].

Multiple kinds of MXenes have been successfully synthesized via etching and exfoliating various MAX phases, such as $Ti_3C_2T_x$, V_2C , Nb_2C , Nb_4C_3 , Ti_4N_3 , and Mo_2C [15–19]. The MAX phases belong to the hexagonal system, which are a new ternary layered compound. The special crystal structure endows MAX phases with excellent performance of both ceramics (high modulus, corrosion resistance, etc.) and metals (excellent electrical conductivity, thermal conductivity, etc.) [20]. After etching by an HF aqueous solution, pristine MXenes retain the hexagonal crystal structure of the MAX phase, the P63/mmc space group. The crystal pattern of MXenes is a hexagonal dense packing structure, wherein transition metal atoms M are arranged in the outer layer, and C (or N) atoms sandwiched between two layers

✉ Lu Shao
shaolu@hit.edu.cn

¹ MIIT Key Laboratory of Critical Materials Technology for New Energy Conversion and Storage, State Key Laboratory of Urban Water Resource and Environment (SKLUWRE), School of Chemistry and Chemical Engineering, Harbin Institute of Technology, Harbin 150000, China

of M atoms (Fig. 1). Transition metal atoms M and C/N atoms are alternately arranged in the order of M/X···/M and the C/N atoms are located in the center of the octahedron formed by the transition metal atoms [21–23]. According to density functional theory (DFT) calculations, the surface groups of MXene may be directly distributed above the hole among the three outermost transition metal atoms or above the C atoms [24–26]. In addition, Xie et al. [27] proved that the surfaces of HF-etched MXenes are mostly covered by –OH terminations through the combination of DFT calculations and experiments. More importantly, the experimental results indicated that an annealing treatment could lead to a surface with fewer –OH and –F groups and accelerate the formation of terminal oxygen-containing MXene layers.

Given their unique advantages of 2D geometry and ultrathin thickness, MXenes could stack into a film, sheet-by-sheet. Compared with conventional films, MXene films have many distinct properties, such as unique optical, mechanical, electromagnetic, and gas-sensitive properties. As a result, MXenes have triggered breakthroughs in many fields [28]. Considering that the number of reports on MXene films has recently grown, this review mainly focuses on the preparation method, application, and working mechanism of MXene films. The MXene synthesis section first summarizes the classic HF etching method and some advanced synthesis techniques reported recently, which involve synthesis method for multiple types of MXenes (instead of a single $Ti_3C_2T_x$). Then various assembly methods of MXene films are introduced, including the most commonly used vacuum-assisted filtration and spin-coating methods, as well as the recent development of electrostatic spinning, hot pressing, and electrodeposition approaches. Finally, the applications of MXenes in energy storage, membrane separation, electromagnetic interference (EMI) shielding, and other emerging applications are summarized. The purpose of this review is to provide a comprehensive illustration of the latest synthesis methods and the state-of-the-art applications of MXenes,

as well as the working mechanism proposed by the representative works.

Brief Overview of the Synthesis Methods for MXene

MXene, as common 2D material, has the inherent advantages of 2D materials, such as a high specific surface area and high processability, though it cannot be obtained in the same way as other 2D materials [29, 30] because of the strong metallic bonds between the “M” and “A” elements. In early studies, strong acids (i.e., an HF aqueous solution) were used to break the Ti–Al bonds, and the Al-element layers were selectively removed to produce multilayered Ti_3C_2 flakes after further exfoliation. MAX phases are a large family, and the successful synthesis of Ti_3C_2 introduces the possibility of etching of multiple MAXs. Most of the synthesis methods mainly depend on water as the main solvent and fluoride-based compounds as etchants for selective etching, which can produce poisonous gases, intercalated water, and abundant hydroxyl groups on the MXene surfaces [27]. To avoid these issues, novel methods have emerged to make the exfoliation process more effective, greener, and with abundant terminations-containing MXenes, mainly including fluoride-containing acidic solutions and its derivative methods [23, 31, 32], chemical vapor deposition (CVD) methods [33, 34], hydrothermal synthesis [32, 35], and alkali etching methods [36, 37]. Nevertheless, acid etching and its derivative methods are still widely used in current research. The etching agents and synthesis method will directly affect the morphology, surface groups, and structural defects of MXenes [38]. Additionally, the properties of MXenes can be tuned by the types and ratios of M to X elements. Furthermore, the advanced characterizations of the MXene-based materials further reveal their potential properties, which facilitate and guide their studies and processing.

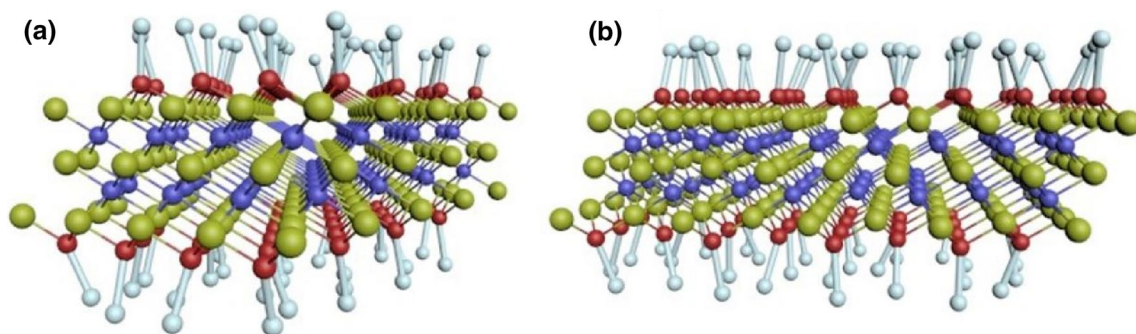
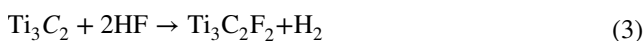
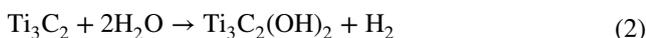
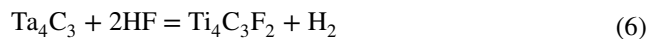
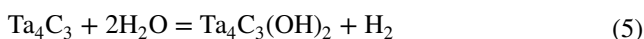


Fig. 1 Structure diagram of $Ti_3C_2T_x$. **a** Left view of $Ti_3C_2T_x$. **b** Front view of $Ti_3C_2T_x$. The white, red, blue, and yellow balls represent H, O, C, and Ti atom, respectively

Unlike graphite layers maintained by weaker Van der Waals forces, the adjacent layers of MAX are held together by strong covalent bonds or metal bonds. As a result, it is difficult to etch directly by a conventional etchant to produce T_3C_2 sheets. Two-dimensional MXene sheets were not successfully achieved until the Ti_3AlC_2 powders were added to a concentrated HF solution by Gogotsi's group [23]. By combining geometry optimization and XRD analysis of the treated Ti_3AlC_2 powders, Gogotsi et al. [23] concluded that the Al layers could be dissolved by the HF acid solution and replaced by functional groups (mainly $-F$ and $-OH$), leaving a structure with a chemical formula of Ti_3C_2 . The etching procedure is illustrated in Fig. 2, and the mechanism can be described by the following formulas:



Similarly, Lin et al. [39] successfully fabricated 2D ultrathin Ta_4C_3 MXene sheets with nanosized lateral dimensions using a two-step liquid exfoliation strategy. The etching process can be described as:



Although the HF etching method is widely used in the production of $Ti_3C_2T_x$, its practical application is still severely hindered because of the toxicity and harmfulness of HF [40–43]. Compared with the direct usage of a concentrated HF solution, the in situ produced HF can remove the A atom layers via a similar reaction process, which suggests protons and fluoride ions are necessary for etching Ti_3AlC_2 powders. The in situ HF etching of MAX can produce large fractions of single-layered MXene flakes with high yields. The obtained MXene sheets are usually accompanied by larger sizes and fewer nanometer-size defects, which are important for some applications. For example, large flakes with few defects are more suitable for applications requiring high electrical conductivity [44]. Furthermore, cations (i.e., Li^+ , NH_4^+) in the etching system can intercalate into interlayers to expand the interflake spacing and weaken the interaction between MXene layers, which is conducive to further exfoliation and inhibiting the restacking during the assembly process [31, 45]. Typically, Wang et al. [32] developed a simple hydrothermal method to synthesize multilayered $Ti_3C_2T_x$ and investigated the effects of the ratio of reactants, reaction time, and reaction temperature on the product yield. Compared with the direct HF solution etching method, they introduced Ti_3AlC_2 powders into the NH_4F aqueous solution at 150 °C for 12 h. In that process, NH_4F

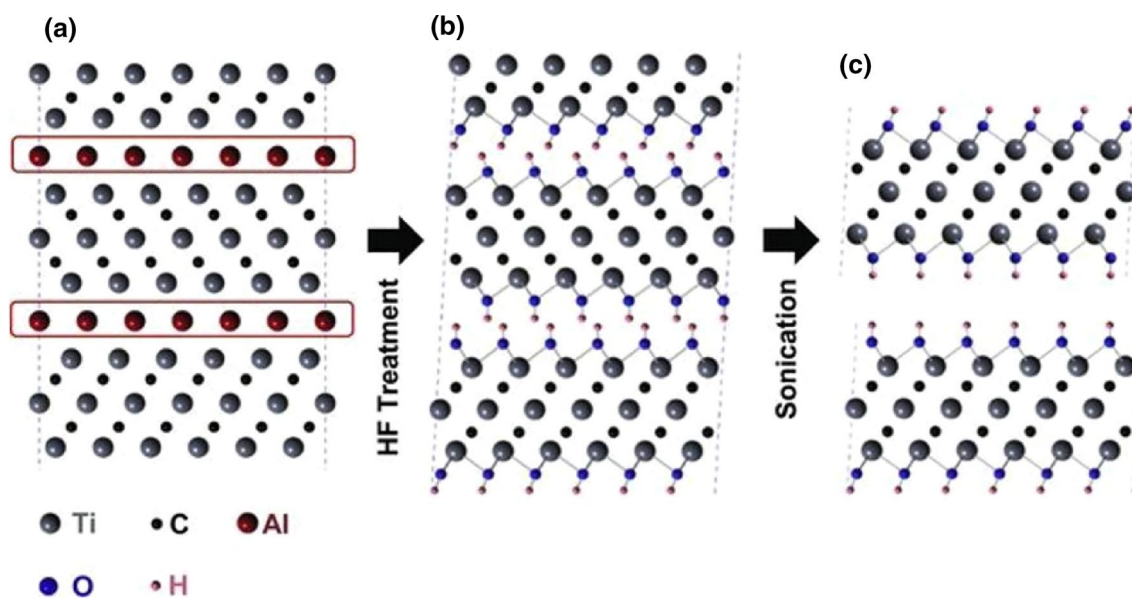


Fig. 2 Structure, exfoliation process of the Ti_3AlC_2 phases and corresponding MXene. **a** Structure of Ti_3AlC_2 . **b** After the HF treatment, Al was replaced by $-OH$ terminations. **c** After ultrasound, the hydro-

gen bonds were broken, and the MXene nanosheets were dispersed in solvent. Reproduced with permission [23]. Copyright 2013, Wiley-VCH

would gradually hydrolyze to produce HF for etching the added powder. $\text{Ti}_3\text{C}_2\text{T}_x$ sheets with a large size (4–15 μm) and defect-free surfaces would be obtained. In addition, a new method with low toxicity and high yield was introduced by Ghidiu et al. [31] to prepare MXene colloidal solution, wherein water was used as the main solvent, HCl, and fluoride salt (LiF in general) as the composite etchant. They first added LiF powders to the HCl solution, followed by the slow addition of Ti_3AlC_2 powders and finally heated in a water bath. Moreover, XRD analysis showed that the layer spacing between sheets in the MXene films produced by a mixed etching agent was larger than that by HF etching, and yields were also higher because of water and/or cations (Li^+) intercalation in hydrophilic and negatively charged MXene sheets. Additional studies with this compound etching agent demonstrated that the ratio of LiF and sonification

treatment (or absence) heavily affect the defect and lateral size of the MXene sheets [46, 47]. Unlike the previously reported method using water as a main solvent, Michel et al. [45] developed a route to fabricate $\text{Ti}_3\text{C}_2\text{T}_x$ MXenes rich in fluorine terminations by etching the MAX phase in a variety of polar solvents with NH_4HF_2 (Fig. 3a, b). Ti_3AlC_2 powders etched by NH_4HF_2 in different organic solvent systems displayed a typical accordion-like morphology, and the TEM micrograph indicates delaminated $\text{Ti}_3\text{C}_2\text{T}_x$ flakes after sonification, confirming the successful synthesis of $\text{Ti}_3\text{C}_2\text{T}_x$ (Fig. 3c, d). The d-spacing of the obtained MXenes was also significantly larger than that of samples etched in an NH_4HF_2 aqueous solution because of the intercalation of NH_4^+ /organic solvent molecule complexes [48]. Another interesting trait of these exfoliated $\text{Ti}_3\text{C}_2\text{T}_x$ flakes is the rich distribution of $-\text{F}$ terminations [approximately 70% for those

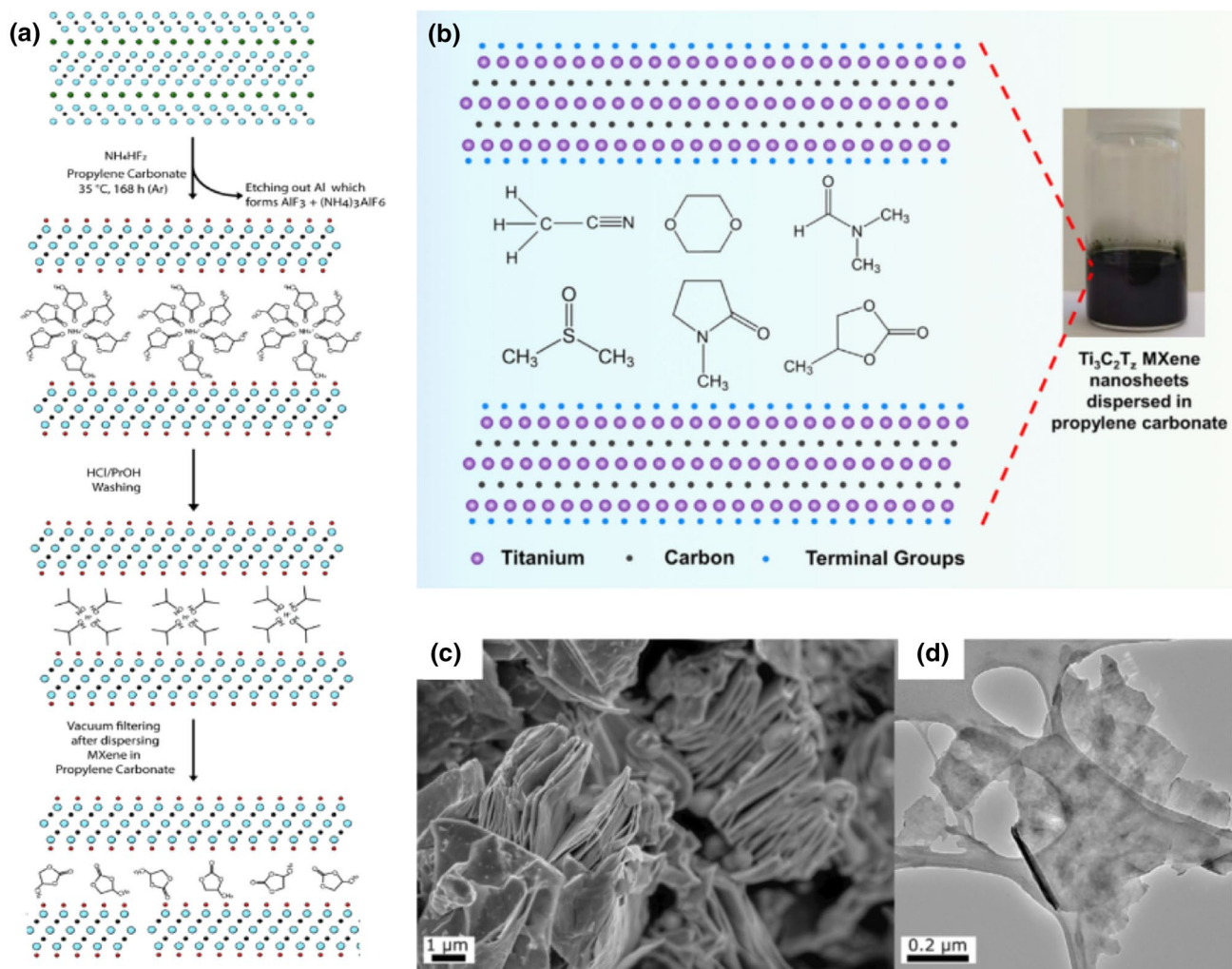
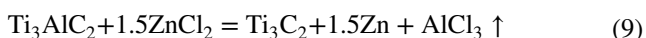
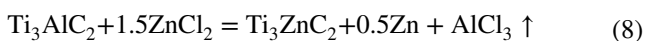


Fig. 3 **a** Flow chart of water-free fabrication of MXene using NH_4HF_2 in organic solvent. Reproduced with permission [45]. Copyright 2020, Cell Press. **b** Supplementary instruction to Fig. 3a, schematic illustration of $\text{Ti}_3\text{C}_2\text{T}_x$ delaminated flakes that were dispersed

stably in several organic solvents. Reproduced with permission [50]. Copyright 2020, Cell Press. **c** Typical SEM micrograph of multilayered $\text{Ti}_3\text{C}_2\text{T}_x$. **d** TEM micrographs of delaminated $\text{Ti}_3\text{C}_2\text{T}_x$ sheets. Reproduced with permission [45]. Copyright 2020, Cell Press

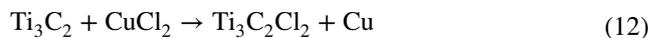
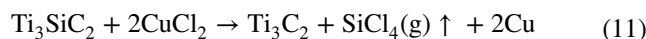
produced in propylene carbonate (PC)], which originated from the NH_4HF_2 in a water-absent environment. Other studies have indicated that water plays the key role in inducing degradation of $\text{Ti}_3\text{C}_2\text{T}_x$ and other MXenes [49]. Therefore, the water-free method may be an alternate synthesis technique for MXene to avoid degradation. More importantly, when MXene exfoliated in propylene carbonate was used as an anode of Na-ion battery, nearly double capacity in a PC-containing electrolyte was observed compared with that when MXene etched in water.

MXenes can also be obtained through an element replacement approach in Lewis acid melt salts. For example, Li et al. [20] synthesized Zn-containing MAX phases (Ti_3ZnC_2 , Ti_2ZnC , Ti_2ZnN , and V_2ZnC) and further fabricated $-\text{Cl}$ terminated MXenes ($\text{Ti}_3\text{C}_2\text{Cl}_2$ and Ti_2CCl_2) based on this method with original materials of Ti_3AlC_2 and ZnCl_2 . In the case of Ti_3ZnC_2 , the synthesis mechanism of the Zn-containing MAX phase can be presented by the following reactions:



Coordinately unsaturated Zn^{2+} can act as Lewis acids because of its strong acceptance of $-\text{Cl}$ and electrons. Weakly bonded Al atoms in Ti_3AlC_2 can be easily oxidized into Al^{3+} and then further bonded with $-\text{Cl}$ to form AlCl_3 [Reaction (9)]. The produced AlCl_3 has a low boiling point (approximately 180°C), which easily escapes from the original system at high temperature (550°C). Ti_3ZnC_2 can be formed as in situ reduced Zn atoms intercalated into the Ti_3C_2 layers and fills the A sites of the MAX phase

previously occupied by Al atoms [Reaction (10)]. The phase evolution of the reaction product is under the influence of multiple pathways, most notably the different $\text{Ti}_3\text{AlC}_2/\text{ZnCl}_2$ ratios. Starting with Ti_3ZnC_2 , the final products can become $\text{Ti}_3\text{C}_2\text{Cl}_2$ with an increasing ZnCl_2 ratio in the original materials. Therefore, a two-step formation process is proposed: the generation of Ti_3ZnC_2 and etching in excess ZnCl_2 (Fig. 4a). Similarly, Fashandi et al. [51] fully replaced the Si atomic layers in Ti_3SiC_2 with a noble metal (Au and Ir) using a solid-state diffusion process at high annealing temperature. Moreover, the separation of Si and Au can be achieved via a thermodynamic drive force at an appropriate temperature. The successful synthesis of the new MXene suggests that the exchange mechanism between the A atomic layer in the MAX phase and metal halide may become a common method for the synthesis of unexplored MXenes with functional A-site elements. Similarly, Huang et al. [52] proposed a more general strategy to synthesize MXenes using direct redox coupling between cations in Lewis acid molten salts and element A at high temperatures. This method successfully generalized the Lewis acid melt salts etching strategy to a variety of chloride salts (i.e., ZnCl_2 , FeCl_2) and unconventional MAX phases with A elements Si, Zn, and Ga. The exfoliation process can be illustrated in Fig. 4b. In this study, the synthesis of MXene was performed with Ti_3SiC_2 as the precursor and CuCl_2 molten salt as the etchants. The reaction between Ti_3SiC_2 and CuCl_2 at 750°C involves the following reactions:



The redox potential of Cu/Cu^{2+} is -0.43 eV in the molten salt system at 750°C . Therefore, the ionized Cu^{2+} in the

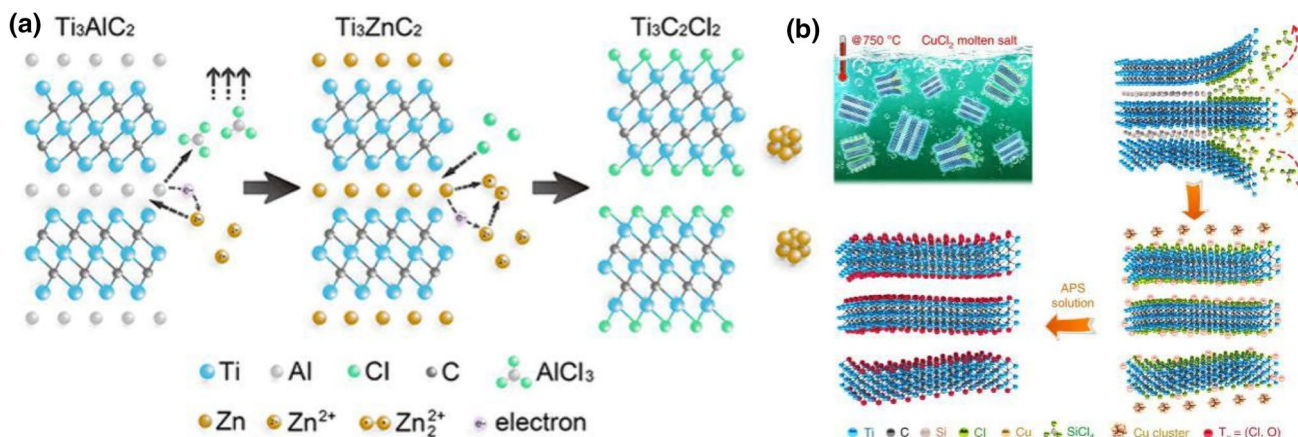


Fig. 4 Schematic of the preparation of MXene by a molten salt method. **a** Synthesis diagram of $-\text{OH}$ and $-\text{Cl}$ terminated MXenes from Ti_3AlC_2 and ZnCl_2 . Reproduced with permission [20]. Copy-

right 2019, American Chemical Society. **b** Synthesis of $\text{Ti}_3\text{C}_2\text{T}_x$ MXene from Ti_3SiC_2 and CuCl_2 . Reproduced with permission [52]. Copyright 2020, Nature Publishing Group

molten salt can easily oxidize the Si atoms to Si^{4+} , Si^{4+} eventually forms SiCl_4 gas with $-\text{Cl}$ to escape from the Ti_3C_2 sublayer, and Cu^{2+} is reduced to Cu element [Reaction (11)]. After Cu is removed by washing with subsequent ammonium persulfate solution, $\text{Ti}_3\text{C}_2\text{T}_x$ MXene with $-\text{Cl}$ and $-\text{O}$ as surface groups can be prepared.

Compared with the molten chloride salt etching methods mentioned above, Urbankowski et al. [18] synthesized Ti_4N_3 MXene using molten fluoride salts (KF, LiF, NaF) to remove the Al layers in Ti_4AlN_3 at 550°C under an argon atmosphere. Further delamination of the multilayered $\text{Ti}_4\text{N}_3\text{T}_x$ via probe sonication produced few-layered and single-layered flakes (Fig. 5). However, there are still some shortcomings in etching the MAX phase in molten salt. First, it is difficult to completely remove the fluoride

and other residues. In addition, the key to most molten salt etching systems is atmosphere protection and temperature control. If the temperature is too high or heated directly in the air, the product may have a cubic phase structure [53].

Since it is difficult to use the transition metals Zr and Hf to form the MAX phase, the corresponding MXenes can be obtained from selectively etching a series of non-MAX phases. The non-MAX phase possesses a similar composition to the MAX phase, while its structure is different from the other known MAX phases. Zhou et al. [54] produced high-purity layered $\text{Zr}_3\text{Al}_3\text{C}_5$ compounds by an in situ reactive pulsed electric current sintering (PECS) process and as a precursor to be exfoliated by HF acid (Fig. 6a). In this process, the relatively weak Al-C bonding units can be easily broken. The following simplified chemical reactions can describe the etching process of $\text{Zr}_3\text{Al}_3\text{C}_5$:

Fig. 5 Fabrication of $\text{Ti}_4\text{N}_3\text{T}_x$ sheets via molten salt treatment of Ti_4AlN_3 at 550°C , the multilayered MXene, and finally single- or few-layered sheets after sonication. Reproduced with permission [18]. Copyright 2016, Royal Society of Chemistry

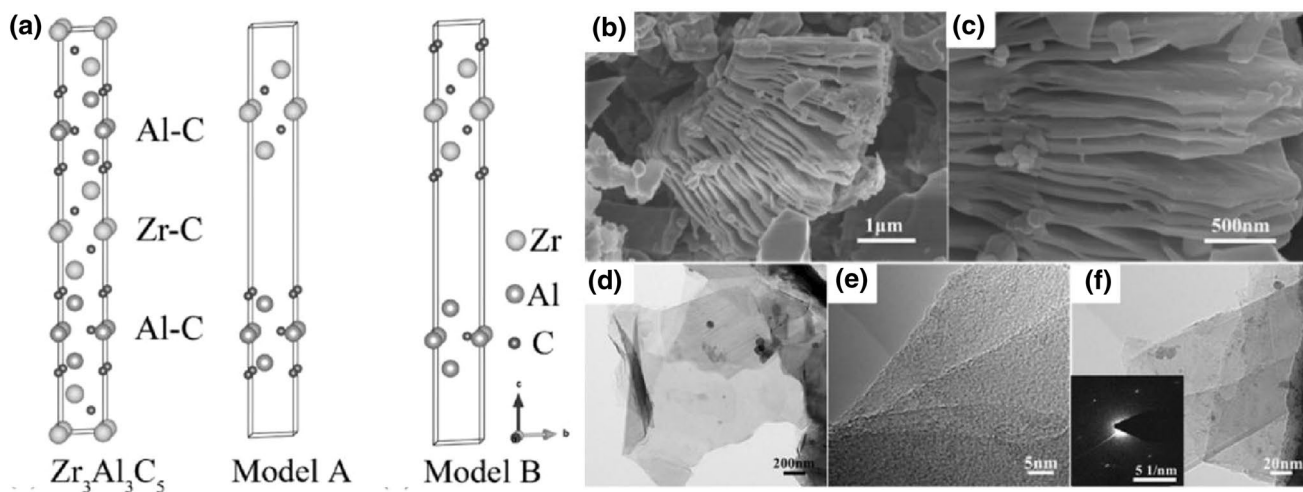
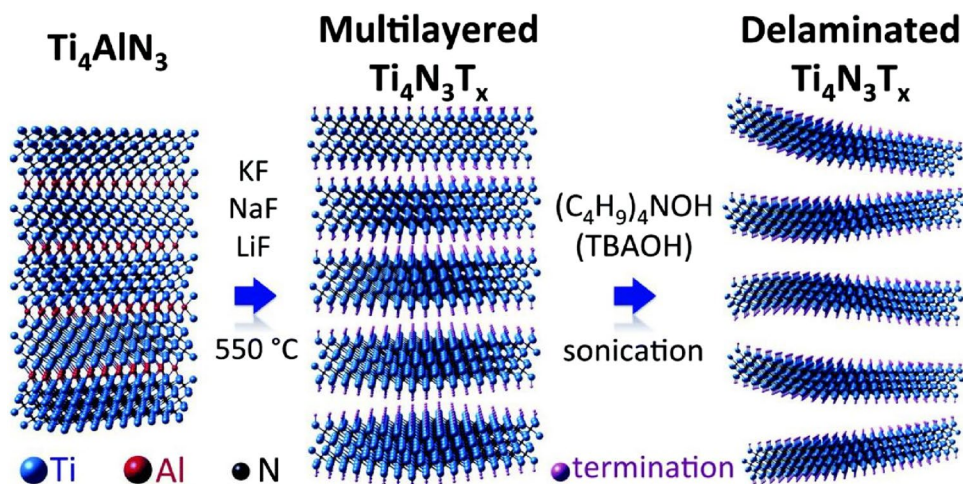
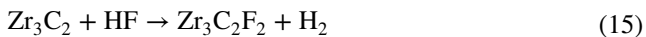
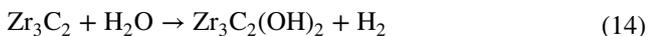


Fig. 6 **a** Crystal structure of parent $\text{Zr}_3\text{Al}_3\text{C}_5$ and corresponding models. **b**, **c** SEM images of the HF-treated $\text{Zr}_3\text{Al}_3\text{C}_5$ powders, exhibiting the accordion-like structure. **d** Typical TEM images of exfoliated 2D $\text{Zr}_3\text{C}_2\text{T}_z$ sheets via ultrasonic treatment. **e**, **f** TEM images of few-layered

$\text{Zr}_3\text{C}_2\text{T}_z$ and rolled $\text{Zr}_3\text{C}_2\text{T}_z$ nanosheets. The inset in **(f)** is a SAED pattern. Reproduced with permission [54]. Copyright 2016, Wiley-VCH



SEM and TEM images revealed the accordion-like structure of HF-treated powders and few-layered $\text{Zr}_3\text{C}_2\text{T}_z$ sheets after ultrasonic treatment, respectively (Fig. 6b–f). Hf-containing layered carbide is more difficult to produce a single phase than Zr-containing carbide through chemical etching the ternary composite Hf–Al–C phase because of the strong interfacial bonding between sublayers. The obtained exfoliation products are mainly cubic phases, usually including $\text{Hf}_3\text{Al}_3\text{C}_5$, $\text{Hf}_3\text{Al}_4\text{C}_6$, and $\text{Hf}_2\text{Al}_4\text{C}_5$ mixed phases [55]. Considering the strong interaction between Hf–C and Al–C layers, it is very important to weaken the interfacial adhesion between Hf–C and Al–C sublayers for further exfoliation. Based on the above experiments and analysis, Zhou et al. [56] introduced a small amount of Si into the Al sites and synthesized $\text{Hf}_2[\text{Al}(\text{Si})_4\text{C}_5]$ and $\text{Hf}_3[\text{Al}(\text{Si})_4\text{C}_6]$ layered parent compounds by PECS process. With the solid solution as the precursor and HF acid as the etching agent, selective exfoliation of the Al(Si)–C structural unit was demonstrated, producing 2D Hf-containing MXenes for the first time (Fig. 7a). The etching mechanism is shown in Table 1 [56]. The representative SEM and TEM images demonstrated the successful etching and exfoliation process (Fig. 7b–e).

To explore the exfoliation mechanism by means of the binding energy and atomic charge calculation, the microscopic mechanism of Si doping facilitating the process of hydrofluoric acid exfoliation was clarified. Since Si has one

Table 1 Chemical equations for etching behaviors and corresponding adhesive energies (in $\text{eV}/\text{\AA}^2$)

Etching progress	Adhesive energy ($\text{eV}/\text{\AA}^2$)
$\text{Hf}_3\text{Al}_4\text{C}_6 \rightarrow \text{Hf}_3\text{C}_2 + \text{Al}_4\text{C}_4$	0.422
$\text{Hf}_3\text{Al}_{3.5}\text{Si}_{0.5}\text{C}_6 \rightarrow \text{Hf}_3\text{C}_2 + \text{Al}_{3.5}\text{Si}_{0.5}\text{C}_4$	0.211
$\text{Hf}_3\text{Al}_{3.5}\text{Si}_{0.55}\text{C}_6 \rightarrow \text{Hf}_3\text{C}_2 + \text{Al}_{3.5}\text{Si}_{0.55}\text{C}_4$	0.283
$\text{Hf}_3\text{Al}_{3.67}\text{Si}_{0.33}\text{C}_6 \rightarrow \text{Hf}_3\text{C}_2 + \text{Al}_{3.67}\text{Si}_{0.33}\text{C}_4$	0.351
$\text{Hf}_3\text{Al}_{3.75}\text{Si}_{0.25}\text{C}_6 \rightarrow \text{Hf}_3\text{C}_2 + \text{Al}_{3.75}\text{Si}_{0.25}\text{C}_4$	0.418

more valence electron than Al, Al can effectively reduce the interface binding energy between the Hf atomic layer and the exfoliated Al (Si) $_4\text{C}_4$ layer from 8.60 to 4.05 eV. Therefore, the introduction of Si has realized the effective tuning of the Hf–C and Al (Si)–C lamellar interface within the unit cell, significantly weakening the interface bonding and introducing efficient exfoliation.

Given that current synthesis methods mainly involve a highly concentrated HF solution or a mixture of fluoride and strong acids for etching the A atomic layers in MAX phases, the produced MXene sheets were normally accompanied by large amounts of –F terminal groups. Although the methods are effective, these processes are environmentally harmful and decrease the material performance (for example, capacitance) because of the chemical inert –F terminals. Several novel studies have revealed that MXenes can also be produced without fluoride by etching their parent MAX phases. Based on the Bayer process, Li et al. [37] proposed a fluorine-free method for etching of the Al element in Ti_3AlC_2 via hydrothermal treatment in 27.5 mol/L NaOH (Fig. 8a). The entire process was totally free of fluorine,

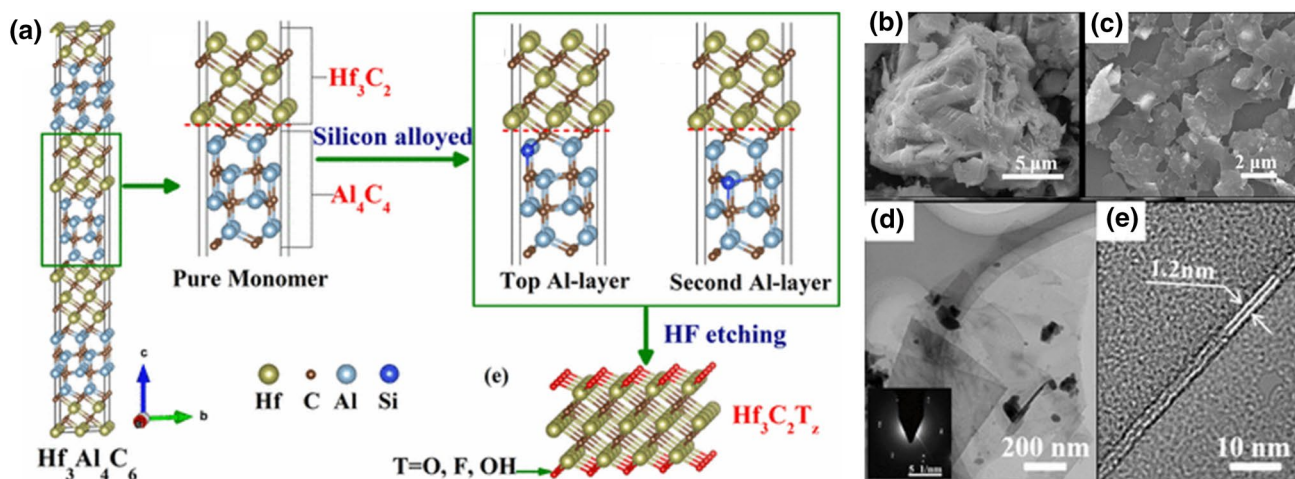


Fig. 7 a Synthesis process of the $\text{Hf}_3\text{C}_2\text{T}_z$ MXene. b SEM images of fabricated $\text{Hf}_3[\text{Al}(\text{Si})_4\text{C}_6]$ powders. c SEM image of powder after HF treatment. d Typical TEM image of the delaminated $\text{Hf}_3\text{C}_2\text{T}_z$ sheets. e

TEM image of few-layered $\text{Hf}_3\text{C}_2\text{T}_z$ sheets. Reproduced with permission [56]. Copyright 2017, American Chemical Society

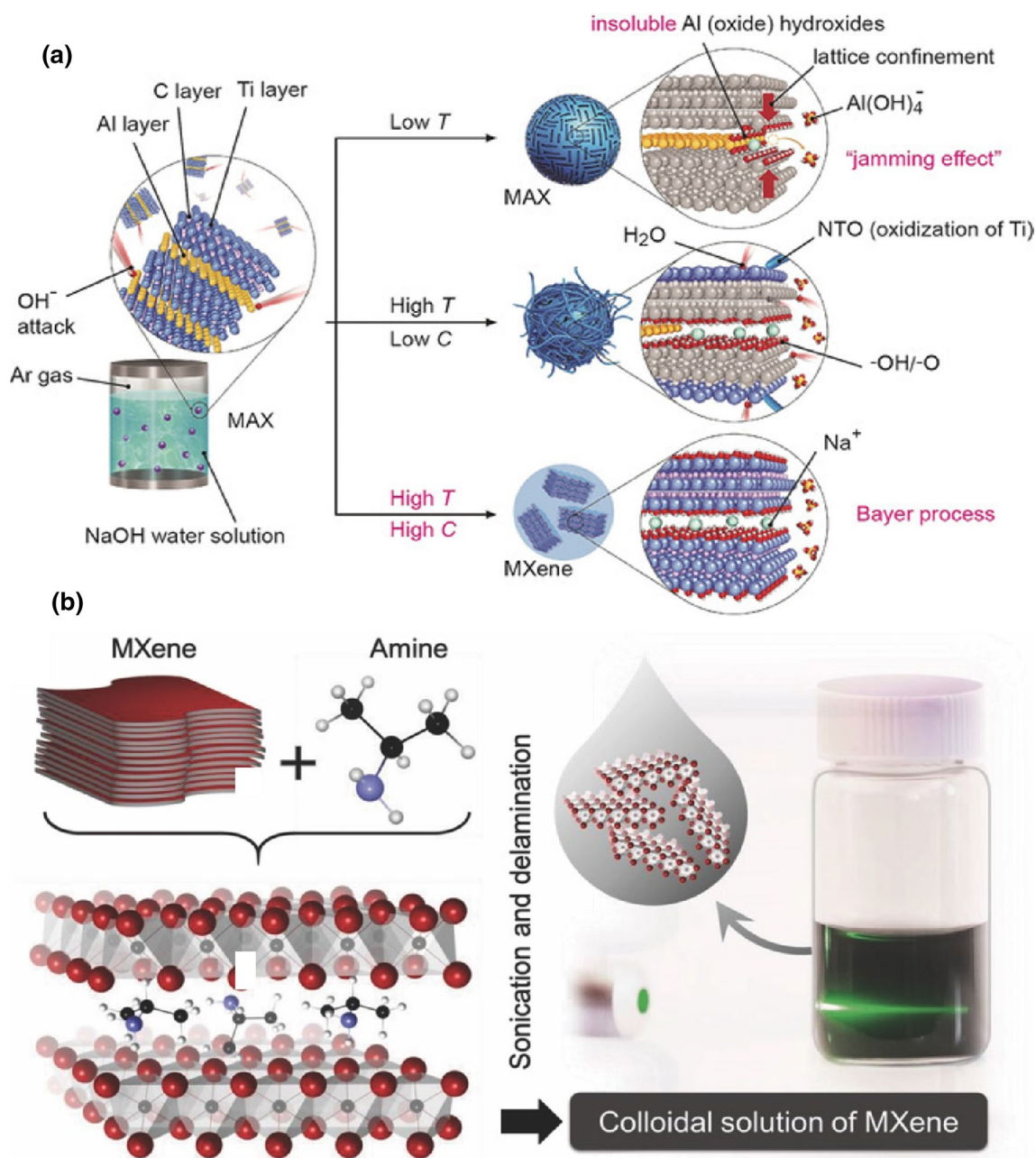


Fig. 8 **a** The etching process of Ti_3AlC_2 in a NaOH aqueous solution under various conditions. Reproduced with permission [37]. Copyright 2015, American Chemical Society. **b** Schematic of the Nb_2CT_x

delamination process via isopropylamine intercalation. Reproduced with permission [64]. Copyright 2015, Wiley-VCH

yielding $-\text{OH}$ and $-\text{O}$ terminated multilayer $\text{Ti}_3\text{C}_2\text{T}_x$ sheets with nearly 92 wt% purity. Moreover, they systematically investigated the effects of temperature and alkali concentration on the etching results. The results showed that the high temperature could accelerate the formation of Ti_3C_2 because the reaction between alkali and undissolved Al hydroxides ($\text{Al}(\text{OH})_3$) is an endothermic process, and the purities of the resulting MXenes are dominated by the alkali concentration. Importantly, the fabricated NaOH- $\text{Ti}_3\text{C}_2\text{T}_x$ thin-film

electrode without $-\text{F}$ terminal groups (thickness 52 μm , density 1.63 g/cm^3) delivered a high gravimetric capacitance value of 314 F/g at 2 mV/s or 254 F/g at 1 A/g, superior to that of HF- $\text{Ti}_3\text{C}_2\text{T}_x$ (100 F/g at 2 mV/s, terminated with $-\text{O}$, $-\text{OH}$, and $-\text{F}$). Similarly, Pang et al. [57] developed an HF-free strategy for synthesizing multiple kinds of MXenes (Ti_2CT_x , Cr_2CT_x , and V_2CT_x) based on a thermally assisted electrochemical etching method. In this paper, we will elucidate the novel process by examining a Ti_2CT_x example in

diluted HCl acid. By adopting carbon fiber cloth and carbon black additives to Ti_2AlC powder to produce a composite electrode, the small voltage (0.3 V vs. RHE is the best) and mild heating caused effective electrochemical etching process. Moreover, the as-synthesized MXene via the HF-free strategy reached 25 μm and a flower-like architecture with a rougher surface than the unetched Ti_2AlC . Such a morphological change indicates effective electrochemical-etching, particularly for the case with a thermal effect.

Excellent properties of 2D materials are only revealed after being delaminated into single or a few atomic layer thicknesses; as a result, the exfoliation process is very important in the preparation of 2D MXene materials [58]. Even after being etched, large amounts of MXene sheets are still restacked because of the presence of hydrogen bonds and electronic attraction [59]. Therefore, the yield of single/few-layered MXene sheets obtained by simple mechanical delamination is relatively low, and delaminated MXene sheets are easy to be oxidized and degraded. Therefore, the subsequent intercalation and delamination process after etching is of significant importance for obtaining single- or few-layered MXene sheets with larger sizes and fewer defects. The post-etched powders are covered with functional groups ($-\text{OH}$, $-\text{F}$, $-\text{O}$, etc.), so MXene flakes are electronegative. Some cations (Li^+ , Na^+ , H^+ , etc.) and/or polar organic molecules (dimethyl sulfoxide (DMSO), N-butyl amine, etc.) can spontaneously intercalate between interlayers because of electrostatic attraction, which is conducive to expanding the interlayer spacing and accelerating the exfoliation of etched samples. Furthermore, the introduction of these guest molecules/ions will also inhibit restacking when exfoliated MXene flakes are further assembled into a film [60–62]. DMSO was effective in delaminating $\text{Ti}_3\text{C}_2\text{T}_x$ MXene while it was not suited for other MXenes [63]. The single- and few-layered 2D $\text{Ti}_3\text{C}_2\text{T}_x$ sheets are generally prepared through the mixture of HF etched powder in a DMSO solution for intercalating the organic compound into the layered structure, and sonication in water under argon atmosphere for delamination. Gogotsi et al. [64] obtained individual 2D Nb_2CT_x sheets via an amine-assisted delamination process and successfully inserted isopropylamine into Nb_2CT_x layers. The schematic of the delamination strategy is shown in Fig. 8b. Isopropylamine is proposed to produce R-NH_3^+ after dissolving in water, and will intercalate into the Nb_2CT_x layers via the electrostatic attraction. In addition, isopropylamine has a three-carbon-atom alkyl tail, which may be small enough to overcome the spatial hindrance of intercalation, and large enough to push the MXene layer away. This approach seems to be more general and has the potential to delaminate $\text{Ti}_3\text{C}_2\text{T}_x$, $\text{Nb}_4\text{C}_3\text{T}_x$, and other MXenes.

In addition to the above-mentioned synthesis methods (or top-down methods), MXenes can also be produced by bottom-up methods such as atomic layer deposition (ALD)

and chemical vapor deposition (CVD). Halim et al. [48] reported the successful deposition of Ti_3AlC_2 thin films from three elemental targets (Ti, Al, C) through direct current magnetron sputtering (DCMC). Using NH_4HF_2 as etchants, the continuous epitaxial Ti_3C_2 thin films could be obtained by selectively removing Al layers, and NH_3 and NH_4^+ were successfully intercalated $\text{Ti}_3\text{C}_2\text{T}_x$ interlayers. A 1 cm \times 1 cm thin film (~ 19 nm) exhibited $\sim 90\%$ light transmittance in the visible-to-infrared range, with a metallic-like nature of the conductivities. CVD can be used to directly synthesize ultrathin MXene material, which is a relatively new method for fabricating MXene-based materials. For example, Xu et al. [33] successfully fabricated 2D ultrathin Mo_2C crystals through a CVD process with a temperature higher than 1085 $^\circ\text{C}$; however, such bottom-up synthesis methods are rarely reported on other MXenes because of the possible bond energies. In this study, methane was used as the carbon source, and a Cu foil sitting on a Mo foil was used as the substrate. The synthesized high-quality 2D ultrathin Mo_2C crystals can reach lateral sizes greater than 100 μm with a few nanometers in thickness. More importantly, the size and thickness of the crystals can be well tuned by varying the experimental conditions, wherein the nucleation density and lateral size can increase with the growing temperature and growing time, respectively.

Although numerous methods have been developed to fabricate various types of MXenes, the current techniques are still restricted by many disadvantages, such as time consumption, heavy pollution, high cost, low yields even on a laboratory scale, low quality, and poor stability. Therefore, the scalable and cost-effective synthesis methods for high-quality MXenes still need to be explored. To realize these goals, attention should be devoted to environmentally friendly etchants and abundantly available inexpensive raw materials. The time of fabrication and yield are also worth considering; as a result, there is a need to focus on fast and easy ways for high yields.

Assembly Technologies of MXene Films

MXenes and their composites have been widely researched in various fields as different forms such as powders [41], films [11], and hydrogels [65]. However, given the increased number of published papers, MXene is still generally assembled into films. For example, MXene films can be applied as flexible electrodes [42, 66], membrane separation (including liquid separation membranes and gas separation membranes) [67, 68], battery separators [69], and molecular sieves [70]. The unique chemical compositions, crystallization structure, and morphology of MXenes have been studied for their potential functionalities. MXene sheets can be assembled into freestanding films using various strategies because of

the strong Van der Waals forces. However, the MXene sheets easily aggregate or restack because of the strong interaction, resulting in the loss of available surface area and active sites [71]. To address this issue, the additional components are introduced into MXene layers to increase the layer spacing, mainly including polymers, carbon materials (carbon nanotubes, graphene, etc.), and other inorganic materials [72–74]. Furthermore, reducing some fluoride and oxygen groups ($-F$, $-OH$, and $-O$) on the surface of $Ti_3C_2T_x$ nanosheets would be contributed to by annealing [75].

Vacuum-Assisted Filtration (VAF)

MXenes can be easily assembled to form interlayer hydrogen-bonded hybrid films through VAF, and a wrinkle-like structure is usually distributed throughout the whole surface of the MXene membrane because of the unique ultrathin

flakes and abundant terminal groups of MXene [76]. Using VAF, substantial efforts have been devoted to fabricating laminar membranes by combining MXene with other materials. As revealed by Ling et al. [77], two kinds of conductive, flexible, high-mechanical strength MXene/polymer composite films were successfully fabricated via VAF. In this work, two polymers were chosen, poly (diallyldimethylammonium chloride) (PDDA) and polyvinyl alcohol (PVA) (Fig. 9a). The former is well cationic polymer that can strongly interact with negatively charged MXene, while PVA has abundant hydrophilic hydroxyl groups along its backbone [78, 79]. The PVA/MXene composite membrane was fabricated by first mixing a MXene colloidal solution (0.3 mg/mL) with a PVA solution (0.1 wt%) in different ratios, followed by ultrasonic treatment to evenly mixed. Finally, the MXene/PVA composite membrane was fabricated by VAF through a polypropylene separator membrane. The as-prepared

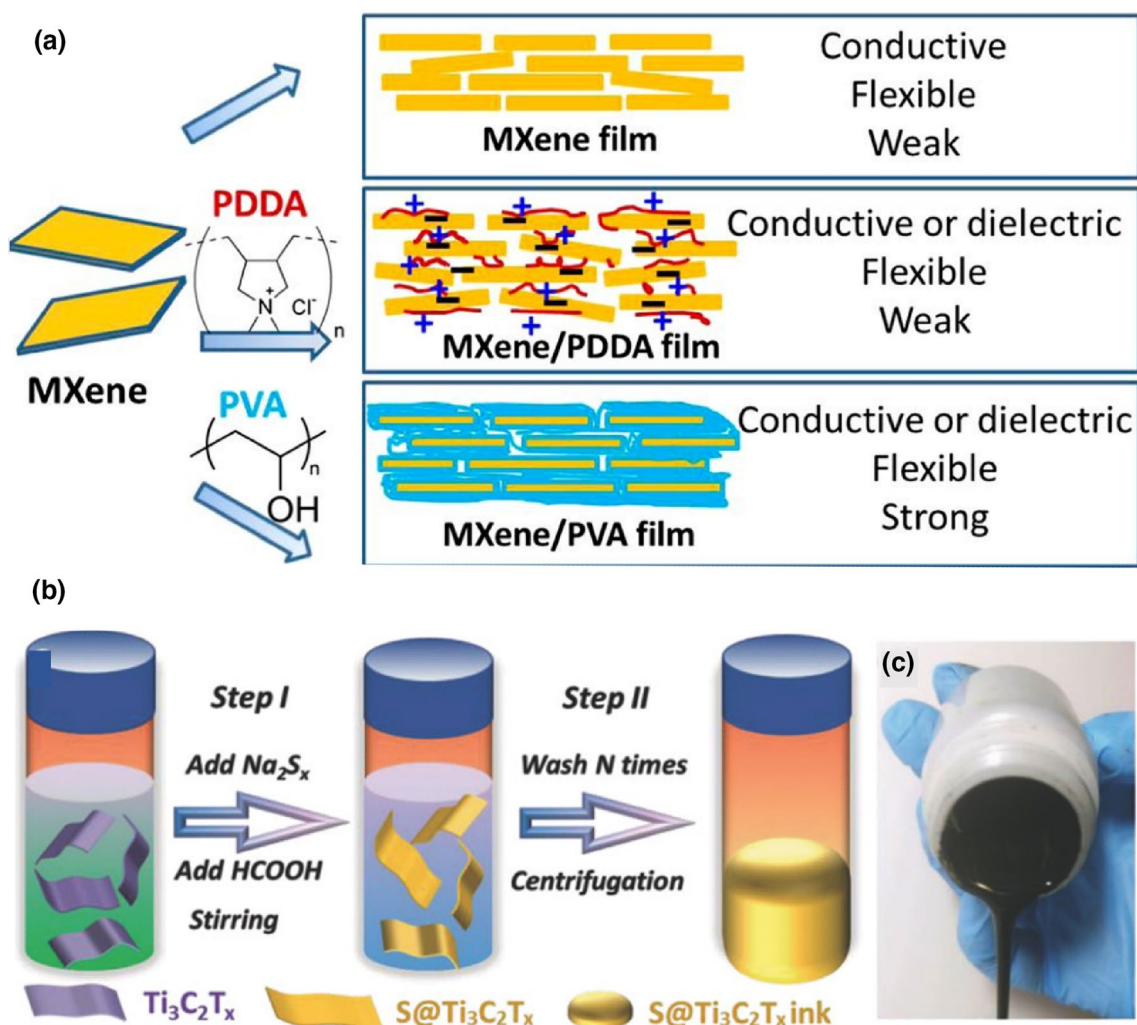


Fig. 9 a Schematic of fabricating different MXene-based films. Reproduced with permission [77]. Copyright 2014, Proceedings of the National Academy of Sciences of the United States of America.

b Schematic and **c** optical image of $S@Ti_3C_2T_x$ ink. Reproduced with permission [81]. Copyright 2018, Wiley-VCH

MXene/PVA composite electrode can achieve a high volumetric capacitance of 530 F/cm^3 at a scan rate of 2 mV/s in 1 mol/L KOH electrolyte and an impressive electrical conductivity as high as $2.2 \times 10^4 \text{ S/m}$. The $\text{Ti}_3\text{C}_2\text{T}_x/\text{PDDA}$ composite films were assembled by the same VAF, which was composed of orderly stacked layers over the entire film. With a similar VAF, Rasool et al. [80] filtrated MXene sheets on the polyvinylidene fluoride (PVDF) membrane to fabricate a water-treatment membrane with anti-biological pollution property. The uniform film coatings on the PVDF exhibited preferred hydrophilicity compared with the pristine PVDF membrane, decreasing the water contact angle to 37° (PVDF was hydrophobic with a contact angle of 81°). The surface roughness of the pristine PVDF and $\text{Ti}_3\text{C}_2\text{T}_x/\text{PVDF}$ membranes was also investigated via AFM. Upon $\text{Ti}_3\text{C}_2\text{T}_x$ coating, the hybrid membrane possessed a rougher surface with wrinkles because of the relatively high pressure exerted on the $\text{Ti}_3\text{C}_2\text{T}_x$ membranes. Tang et al. [81] demonstrated nano-sulfur particles uniformly nucleating and growing on the surface of single-layer or few-layer MXene sheets, and a composite aqueous viscous ink rich in S and MXene sheets was prepared by in situ reduction at room temperature (Fig. 9b). This water-based viscous ink could be further vacuum-filtrated to form high-strength, highly conductive, freestanding, and flexible $\text{S@Ti}_3\text{C}_2\text{T}_x$ composite electrodes without a polymer binder or conductive agents.

Liang et al. [82] reported that carbon nanotubes (CNTs) and MXene could also be assembled into composite films through VAF and used as the electrode of a lithium sulfur battery. Multi-walled CNTs with a diameter of approximately 8 nm were added into the MXene colloidal solution, and the solution was stirred in chlorosulfonic acid. Finally, the suspension was filtered on an anodic aluminum oxide (AAO) membrane and dried at 80°C . The resultant film possessed a conductive porous framework structure, which contained a large number of polysulfides, such that the material had excellent cycling performance. Recently, an ultrathin and highly flexible $\text{Ti}_3\text{C}_2\text{T}_x/\text{CNFs}$ composite paper was prepared by a facile VAF method to induce self-assembly [83]. Through the interaction of 1D CNFs and 2D $\text{Ti}_3\text{C}_2\text{T}_x$, the paper exhibited a high tensile strength (up to 135.4 MPa) and fracture strain (up to 16.7%) while maintaining high conductivity and excellent electromagnetic shielding efficiency.

Utilizing the VAF method, various MXene-based films were successfully fabricated, which further accelerates the exploration for their potential applications. However, the relatively high pressure exerted on films may cause the loss of water-soluble polymers and micro molecules. This will cause significant deviation from the original percent composition of MXene and other materials, which makes it difficult to see the precise relationship between the performance and composition. In addition, the high pressure significantly aggravated the restacking between MXene flakes.

Such self-restacking during VAF has been demonstrated to reduce the accessibility of electrolyte ions and decrease the utilization rate of active sites, thus deteriorating the intrinsic performance of assembled MXene films.

Spin-Coating Method

Spin-coating is widely used to fabricate uniform MXene-based films in a fast and efficient way. Normally, a mixed solution of an MXene colloidal solution and additives is first treated by intense stirring or ultrasound to form a homogeneous solution. The homogeneous solution is then spread on a clean substrate under centrifugal force to allow the solvent to evaporate under high temperature and/or vacuum. Finally, an independent MXene-based composite film can be detached from the substrate for subsequent research [84, 85]. Montazeri et al. [86] fabricated MXene transparent contacts by a simple spin-coating method and applied it to Ti_3C_2 -based MXene photodetectors (Fig. 10a). This transparent MXene film could decrease the trade-off between carrier transmission distance and responsiveness, increased the sensitivity of the photodetectors by four times that of similar devices implemented in gold (Au). Zhang et al. [87] demonstrated a highly transparent, conductive, and ordered $\text{Ti}_3\text{C}_2\text{T}_x$ film as well as its application in transparent and solid-state supercapacitors. The continuous transparent film was obtained via spin-coating $\text{Ti}_3\text{C}_2\text{T}_x$ sheets with a colloid solution, followed by vacuum annealing at 200°C to produce large $\text{Ti}_3\text{C}_2\text{T}_x$ sheets parallel to the substrate. Dillon et al. [88] reported a $\text{Ti}_3\text{C}_2\text{T}_x$ film with a thickness of only a few dozen nanometers and a conductivity up to 6500 S/cm by spin-coating; the fabrication process is shown in Fig. 10b. In this study, the limitations of preliminary optical studies of MXenes carried out by physical vapor deposition were overcome [48]. The resulting high conductivity was attributed to the metal-like free-electron density and highly coplanar arrangement of individual nanomaterials created by spin-coating.

Most reported silicon-based micro supercapacitors (MSCs) still have problems, such as low energy density and a complex manufacturing process, which hinder their integration with silicon chips [89, 90]. To address these disadvantages, Huang et al. [85] proposed a low-cost treating-cutting-coating manufacturing method to fabricate $\text{Ti}_3\text{C}_2\text{T}_x$ MXene-based on-chip MSCs. Spin-coating was employed to deposit conductive $\text{Ti}_3\text{C}_2\text{T}_x$ MXene on a hydrophilically treated Si/SiO₂ wafer. The MXene films produced on the Si/SiO₂ chip are extremely thin, with the thickness ranging from 100 to 600 nm , along with outstanding uniformity and stability. On the basis of these ultrathin MXene membranes, the MSCs produced by this method possessed interdigitated architectures and showed high areal and volumetric capacitance of $472 \mu\text{F/cm}^2$ and 21.4 F/cm^3 , respectively, with a capacitance retention rate greater than 87.6% after $10,000$

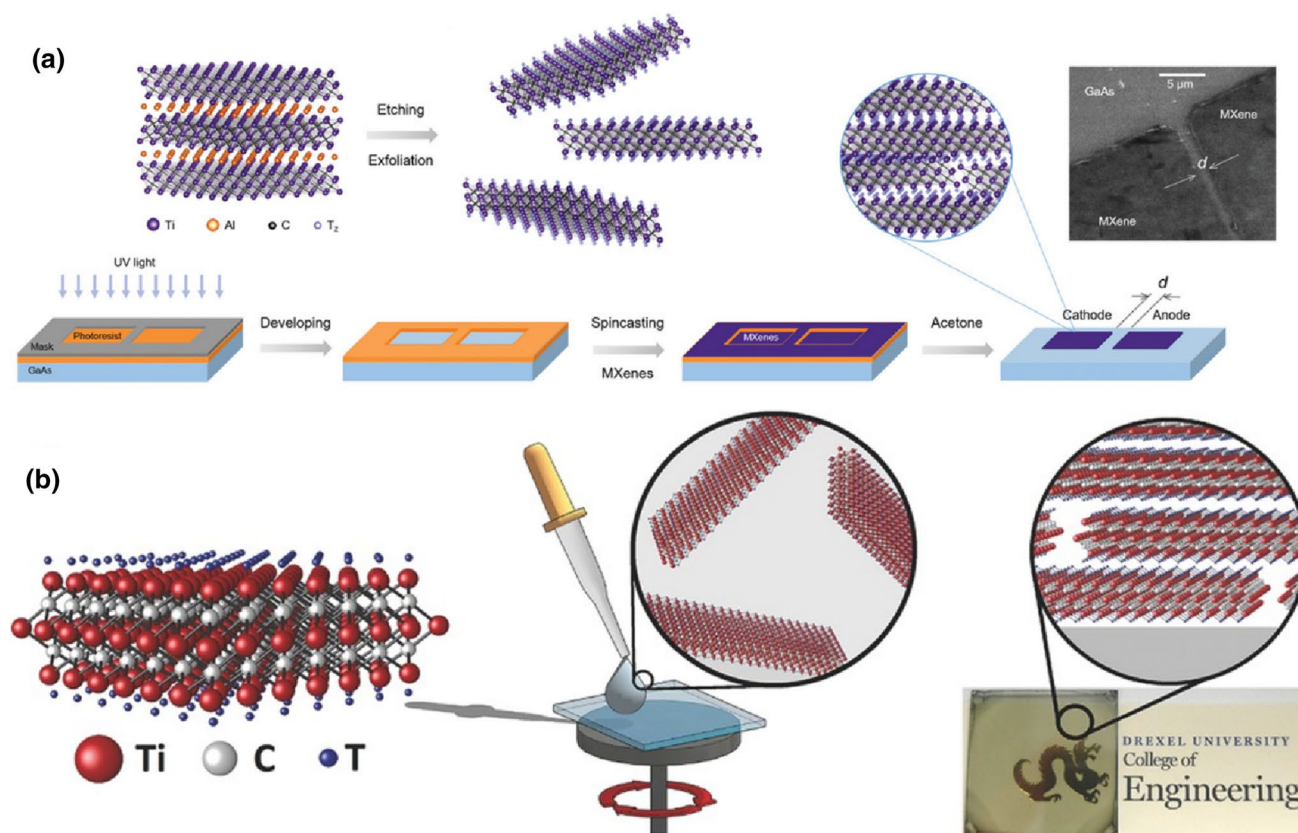


Fig. 10 **a** Fabrication process of the photodetector and SEM image of the final device showing a cathode–anode separation gap. Reproduced with permission [86]. Copyright 2019, Wiley-VCH. **b** Sche-

matic of the $\text{Ti}_3\text{C}_2\text{T}_x$ MXene film prepared by depositing a $\text{Ti}_3\text{C}_2\text{T}_x$ aqueous solution on different substrates via spin-coating. Reproduced with permission [88]. Copyright 2016, Wiley-VCH

cycles. Therefore, this work provides new ideas and strategies for the development of miniaturized and intelligent energy storage devices.

Other Emerging Methods

In addition to commonly used VAF and spin-coating, other methods, such as hot pressing, electrostatic spinning, and electrochemical deposition, have been reported for the preparation of MXene composite films and their features are summarized in Table 2. Since the thermal stability of MXenes is better than that of polymers [91], the preparation of MXene/polymer composite films can be performed by hot pressing above the melting point of the polymers and below the degradation temperature of the MXenes. This method is much more suitable for scale-up production with the advantages of solvent-free, flexible formulation, economical, and environmentally friendly. Sheng et al. [92] proposed a simple and feasible technique to produce MXene/polyurethane (TPU) composite films with superior mechanical and thermal properties via combination melt blending and hot pressing. To avoid restacking of MXene sheets and achieve better

dispersion during the melt blending process, the exfoliated MXene sheets were pretreated with polyethylene glycol to enhance their interactions with hydrophobic TPU polymers. TPU was then blended with the modified MXene flakes, and a series of $\text{Ti}_3\text{C}_2/\text{TPU}$ films were obtained. Ghidui et al. [31] reported a flexible MXene film prepared from MXene conductive clay and fabricated as a flexible electrode to investigate its electrochemical performance. The clay-like paste formed by resultant sediment was rolled into a flexible self-supporting film in a few minutes between water-permeable membranes placed in a roller mill (Fig. 11a).

MXene/rGO composite films were fabricated via electrostatic self-assembly of positively charged reduced graphene oxide (rGO) modified with poly (diallyldimethylammonium chloride) and negative $\text{Ti}_3\text{C}_2\text{T}_x$ flakes [93]. Comparing the random physical mixing, the electrostatic attraction established between MXene and rGO nanosheets effectively prevents the self-restacking of rGO or MXene nanosheets. The enlarged spacing between the MXene flakes accelerated ion diffusion and enabled more electroactive sites to be fully utilized. An interfacial self-assembly method was also used to fabricate thin and laminated MXene films with high stacking

Table 2 Summary of the several assembly techniques

Assembly technique	Advantages	Disadvantages	Application	References
VAE	Simple operation	Time-consuming, aggregation of MXene flakes	Supercapacitors	[97]
Spin-coating	Rapid film forming, well-defined composition	Aggregation of MXene flakes	Photodetectors	[86]
Interfacial self-assembly	High uniformity, rapid film forming	–	Gas sensors	[94]
Electrostatic self-assembly	Ultrathin and controlled thickness	–	Supercapacitors	[93]
Cold press (CP)	Expanded interlayer spacing, well-defined film structure	–	Lithium-ion batteries	[98]
Hot press (HP)	Solvent-free, flexible formulation	Inapplicable to polymers with low degradation temperature or high melting point	Coating, adhesives, etc	[92]
Electrospinning	Structural tunability, progress controllability	–	Oil/water separation	[95]
Electrophoretic deposition	High uniformity, adjustable mass loading	–	Supercapacitors	[99]
Electrochemical polymerization	Controlled reaction rate and thickness	–	Micro supercapacitors	[100]

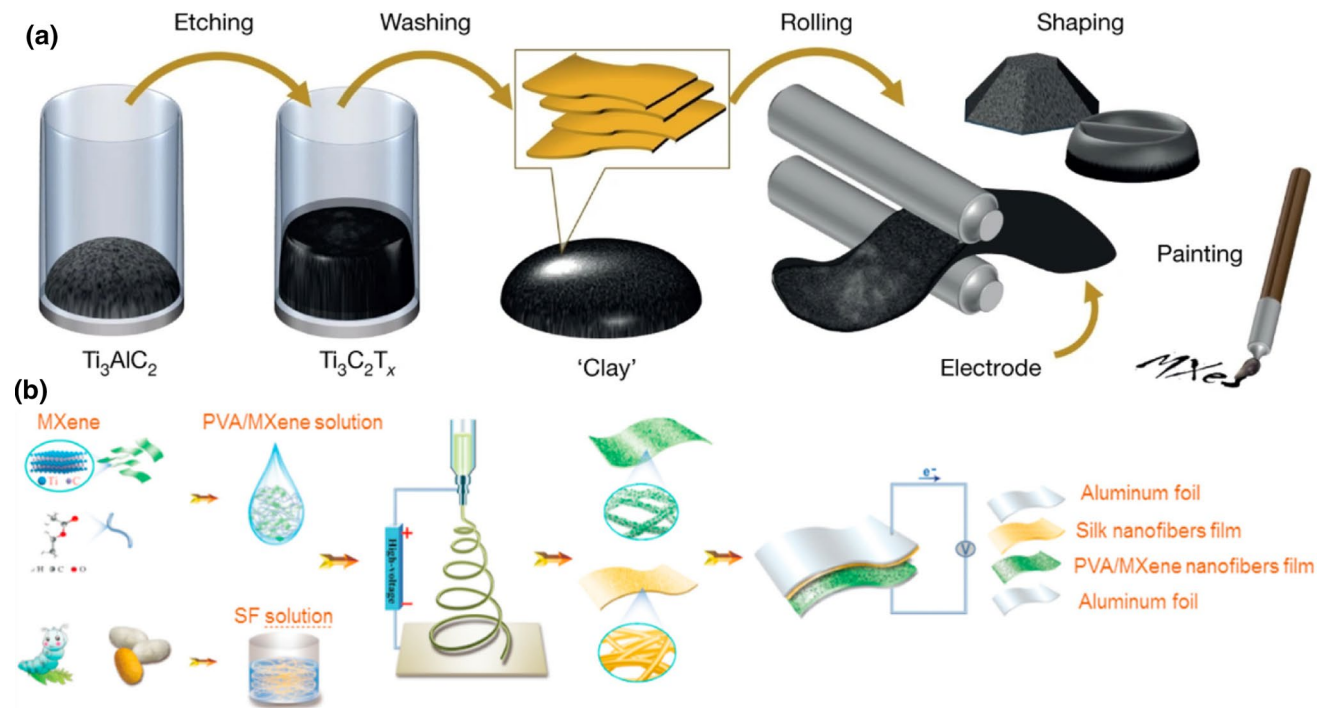


Fig. 11 **a** Fabrication diagram by rolling MXene clay to produce flexible, freestanding MXene films. Reproduced with permission [31]. Copyright 2014, Nature Publishing Group. **b** Preparation process

of PVA/MXene nanofibers film. Reproduced with permission [96]. Copyright 2019, Elsevier

order [94]. The films can typically be assembled within a few minutes, and their thickness is usually 10 nm. To pursue the maximized electrical conductivity of fabricated films, the adherence and density of interflake contacts needed to be optimized. By adding HCl to reduce the pH to 3, the zeta potential was improved to -30 mV, which is necessary to

weaken electrostatic repulsion. In addition, the density of the interlayer contacts can also be modulated by controlling the individual MXene sheet sizes. Furthermore, the slow addition of ethyl acetate to a diluted MXene aqueous solution could accelerate the spontaneous assembly of MXene films on the water surface, which was then easily transferred to a

variety of substrates. The assembled Ti_3C_2 MXene films displayed an average sheet resistance as low as 310Ω at 10 nm thickness because of the reduced surface charges on individual flakes. Electrospinning is a widely applied technique for the manufacture of nanofiber and fibrous films [95], which was also successfully conducted to fabricate PVA/MXene nanofiber films by adding PVA matrix material to $\text{Ti}_3\text{C}_2\text{T}_x$ nanosheets suspension (Fig. 11b) [96]. These MXene-based films achieved enhanced flexibility and were used as the negative friction layer in a triboelectric nanogenerator (TENG). While silk fibroin was chosen as the positive friction layer, the assembled TENG displayed superior mechanical properties and high-power harvesting ability.

Given the unique properties and extensive applications of MXene-based films, researchers have made great efforts to develop new fabrication strategies. One of the most important factors during the assembly process is the dispersion of MXene flakes in colloidal solutions, which has a great impact on optimizing the internal structure of the MXene films. Uniform and closely-integrated MXene-based composite films cannot be formed because of the poor interactions between MXene sheets and other additives. Therefore, more attempts should be made to enhance the interactions between MXene sheets and other materials. This goal can be realized by modifying the charge distribution on the MXene surfaces via surface modification or a charge screening effect. With the increasing emergence of the fabrication methods, materials with various functionalities can be introduced to compound with MXenes and MXene films to obtain a novel internal structure, which will further accelerate their extensive applications in different fields.

Applications and Working Mechanisms of MXene Films

MXene films show great application potential in many fields because of their abundant surface terminations, various compositions, and high hydrophilicity. MXenes and their hybrid films have especially excellent metallic conductivity and high flexibility, making them be widely regarded as potential candidates for flexible electrochemical devices [62]. Additionally, MXene films have extraordinary permeation and highly efficient selection properties that result from the regular sub-nanometer channels and abundant surface-terminating groups on the MXene nanosheets and are novel materials in the gas separation and liquid separation fields. In addition, MXenes also possess characteristics, such as high specific surface area, easy absorption of electromagnetic radiations, and controllable thickness, which are attractive to fields of EMI shielding and solar desalination. Although MXene films have been widely investigated in many fields, some crucial problems still exist, such as time consumption

and poorly understood mechanisms, which greatly limit their practical applications. To overcome these drawbacks, many researchers have made innovative improvements in MXene films. In this section, we summarize the main applications of MXene films, and simultaneously highlight the correlations between compositions, structure, and performances.

Energy Storage

MXenes, promising energy storage materials, have been mainly investigated in batteries and supercapacitors [101–103]. Theoretical research combining with many experiments showed that the electrical properties of MXenes are similar to those of metals and semiconductors, which is related to their elemental composition and surface terminal groups [104]. Ideal pristine MXenes are metallic; however, they can be turned into semiconductors after surface functionalization. Similar to other 2D materials, both organic/inorganic molecules and various ions can spontaneously perform intercalation between MXene layers, which offers a larger surface area for charge storage and provides an attractive pathway to enhance the conductivity of layered materials by increasing the carrier concentration. MXenes also have broad application prospects in flexible consumer electronics because of the graphene-like flexibility and metal-like electric conductivity [105–108]. Additionally, a great deal of effort has been devoted to improving the electrochemical performances of MXene-based films [109, 110]. However, pristine MXene films still cannot meet the requirements of practical applications because of the easy-stacking between sheets, lack of mechanical strength, and relatively low energy density. Therefore, MXenes are usually compounded with other materials (polymers, inorganic materials, etc.) to fabricate composite films or loaded onto various substrates. Another strategy is to tune the internal structure of MXene films to increase the ion transport, thus improving the energy storage performance. Various innovative methods and research on the electrochemical performance improvement of MXene films appeared in response to these problems. Therefore, we subdivide this literature into two major topics: (1) supercapacitors and (2) batteries. For supercapacitors, we mainly analyze the studies focused on MXene-based composite electrodes and the corresponding construction of ion transport channels. For batteries, we highlight Li–S batteries, Na-ion batteries, Li-ion batteries, and their corresponding stimulations. Their electrochemistry performance can be seen in Table 3.

Supercapacitors

The increasing miniaturization and portability of wearable consumer electronics has stimulated the rapid development of supercapacitors [111–113], which play an important role

Table 3 Comparison of MXene-based films in applications of supercapacitors and batteries

MXene-hybrid film	Synthesis method	Assembly technique	Application	Current density	Capacitance/capacity	References
Ti ₃ C ₂ T _x	HCl + LiF	Rolling	Supercapacitors	2 mV/s	900 F/cm ³	[31]
Ti ₃ C ₂ T _x /SWCNT	HF etching	VAE	Supercapacitors	2 mV/s	390 F/cm ²	[97]
Ti ₃ C ₂ T _x /rGO	HF etching	VAE	Supercapacitors	2 mV/s	435 F/cm ²	[97]
Ti ₃ C ₂ T _x /antimonene	HF etching	VAE	Supercapacitors	0.5 mA/cm ²	4255 F/cm ³	[123]
Mo _{1.33} C/PPy	HF etching	Electrochemical polymerization	Supercapacitors	0.2 mA/cm ²	333.9 F/cm ³	[100]
Ti ₃ C ₂ /PDDA	HF etching	VAE	Supercapacitors	2 mV/s	296 F/cm ³	[77]
Ti ₃ C ₂ /PPy	HCl + LiF	VAE	Supercapacitors	5 mV/s	1000 F/cm ³	[143]
Ti ₃ C ₂ T _x /BC	HCl + LiF	VAE	Supercapacitors	3 mV/s	2084 F/cm ²	[110]
Ti ₃ C ₂ T _x	HCl + LiF	Spin-coating	Micro-supercapacitors	1.0 μA/cm ²	470 μF/cm ²	[85]
Ti ₃ C ₂ T _x /rGO-PDDA	HCl + LiF	Electrostatic self-assembly	Supercapacitors	2 mV/s	1040 F/cm ³	[93]
Ti ₃ C ₂	HF etching	VAE	Li-ion batteries	1 C	410 mA·h/g	[60]
Mo ₂ TiC ₂	HF etching	VAE	Li-ion batteries	1 C	176 mA·h/g	[144]
Ti ₃ C ₂ /PEDOT	HCl + LiF	VAE	Li-ion batteries	100 mA/g	295 mA·h/g	[137]
Ti ₃ C ₂ T _x	HCl + LiF	CP	Li-ion batteries	0.1 C	295 mA·h/g	[98]
Ti ₃ C ₂ /rGO	HF etching	VAE	Li-ion batteries	0.05 A/g	336 mA·h/g	[145]
Ti ₃ C ₂ T _x /CNT	HF etching	VAE	Li-ion batteries	0.1 C	1250 mA·h/g	[146]
Ti ₃ C ₂ T _x /S	HCl + LiF	VAE	Li-S batteries	0.1 C	1383 mA·h/g	[109]
Ti ₃ C ₂ T _x /S	HCl + LiF	VAE	Li-S batteries	0.1 C	1029.7 mA·h/g	[113]
Ti ₃ C ₂ T _x	HCl + LiF	VAE	Na-ion batteries	2.5 C	295 mA·h/g	[141]
Mo ₂ CT _x	HCl + LiF	VAE	Na-ion batteries	2.5 C	290 mA·h/g	[141]
PDDA-BP/Ti ₃ C ₂	HCl + LiF	Electrostatic self-assembly	Na-ion batteries	0.1 A/g	1112 mA·h/g	[140]

in our daily life with their long cycle life, charging/discharging rates, and high energy density. Supercapacitors comprised of novel electrode materials have caused widespread attention in recent years and are thought to affect the development of next-generation electronic devices well. MXene films are attractive as advanced electrodes in supercapacitors given their high electric conductivity, excellent mechanical property, and Faraday pseudocapacitive charge storage mechanism [114, 115]. Theoretically, the functionalization of -F and -OH on the surface of MXenes may contribute to its mechanical tensile stress, which enables MXene films to have much better tolerance to both biaxial and uniaxial tension than graphene because the surface functionalization can suppress the breakdown of atomic layers and enhance the mechanical elasticity [116]. Alternatively, the Faraday pseudocapacitance is derived from changes in the oxidation states of surface Ti atoms, which is caused by the reversible insertion/distraction of protons and is not diffusion-limited [31, 117].

Ti₃C₂T_x, one of the most studied MXene materials, has been extensively used in supercapacitors. Studies demonstrate that a self-supported Ti₃C₂T_x film electrode can deliver a volumetric capacitance of 300–400 F/cm³ in neutral or alkaline electrolytes, which is greater than those of most carbon-based double-layer capacitors and comparable to

graphene electrode [118, 119]. In early research, Ghidiu et al. [31] crushed the clay-like MXene into films as the electrode of supercapacitors (Fig. 12a). When H₂SO₄ solution was used as the electrolyte, the volumetric capacitance and gravimetric capacitance were up to 900 F/cm³ and 245 F/g at 2 mV/s, respectively (Fig. 12b). This increase can be attributed to the smaller size of H⁺ compared with the other intercalating cations, surface redox processes, and larger interlayer spacing between LiF + HCl-etched MXene flakes than the previously HF-etched samples. In addition, this work also analyzed the impact of thickness on the volumetric capacitances. Not surprisingly, thicker electrodes showed decreased capacitance, which is ascribed to poor flake alignment and long ion transport pathways. In addition, the MXene clay is hydrophilic and layered, and water molecules slide between sheets as it hydrates, making it malleable and easy to shape. In order to shorten the ions transport pathways in thicker films, a more innovative and effective method has been proposed, which alters the self-assembly ways of MXene sheets from parallel to the electrode to vertical alignment (Fig. 12c) [120]. However, the study reveals that the colloidal solution of titanium carbide nanocrystals could exhibit long-range orientation similar to that of disc-like liquid crystal molecules; however, the interactions between the nanocrystals were too weak to effectively

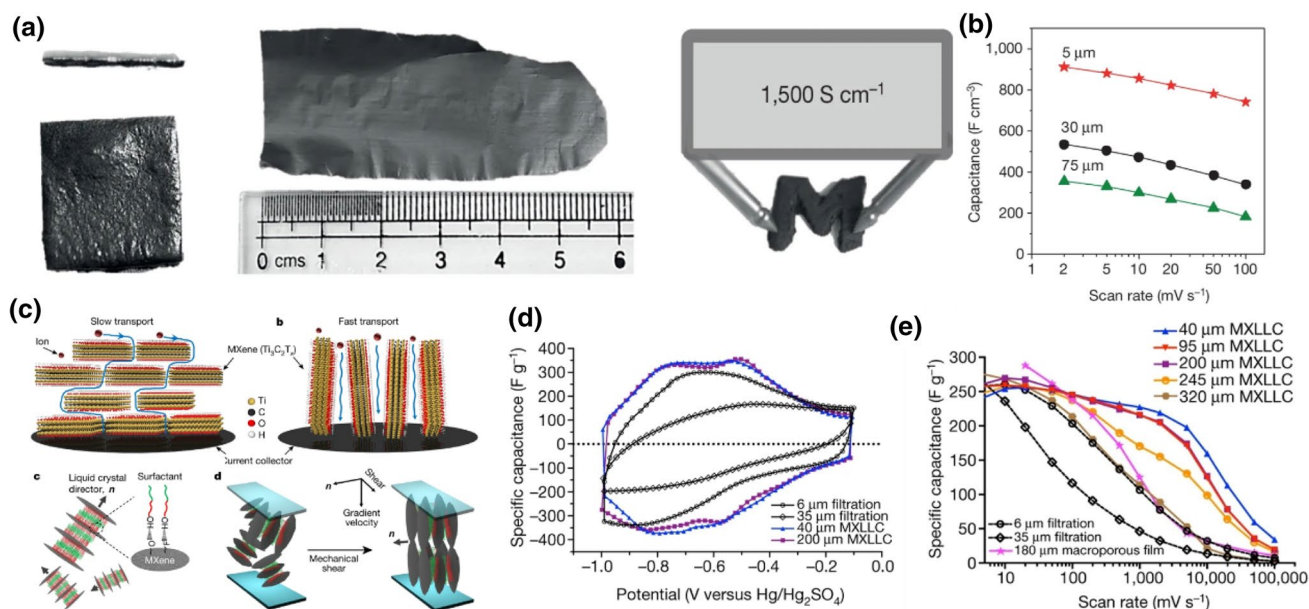


Fig. 12 **a** Images of clay-like MXene and rolled films. **b** Rate performance of rolled electrodes with different thicknesses. Reproduced with permission [31]. Copyright 2014, Nature Publishing Group. **c** Schematic of the vertically aligned $\text{Ti}_3\text{C}_2\text{T}_x$ MXene films. **d** Comparison of the cyclic voltammograms of the indicated samples, including

filtered MXene paper and MXene lamellar liquid crystal (MLLC) films, at a scan rate of 100 mV/s. **e** Rate performance of vacuum filtrated films and MLLC films at scan rates ranging from 10 to 100,000 mV/s. Reproduced with permission [120]. Copyright 2018, Nature Publishing Group

maintain orientation because of the wide distribution of the lateral sizes [121]. The introduced nonionic surfactant (C_{12}E_6) could strongly interact with functional groups (such as $-\text{O}$ and $-\text{F}$) on the surface of MXene to align sheets more orderly, thereby increasing the packing symmetry. In addition, single-walled carbon nanotubes were also added to improve the structural stability and conductivity. Finally, the vertical alignment was obtained by a uniaxial in-plane mechanical shear force to the discotic lamellar liquid-crystal phase. Furthermore, the possibility of using vertically aligned MXene nanosheets as supercapacitor electrodes prepared via VAF was investigated. The results showed that the rate performance of the films has nearly full independence from thicknesses ranging from 40 μm to 200 μm , especially below 2000 mV/s (Fig. 12d, e). The thickness-independent electrochemical performance could be ascribed to the vertically arranged flakes, in which ions can realize directional transport. Kong et al. [122] presented a reduced-repulsion freeze-casting assembly technique via engineering interlayer interactions for constructing 3D porous $\text{Ti}_3\text{C}_2\text{T}_x$ films. To weaken the interlayer repulsion, KOH solution was added to the $\text{Ti}_3\text{C}_2\text{T}_x$ suspension to decrease the electronegativity via functional group substitution and a charge screening effect. Notably, the porous pseudocapacitor electrodes delivered a high capacitance of 358.8 F/g at 20 mV/s, higher than that of filtered $\text{Ti}_3\text{C}_2\text{T}_x$ film (251.5 F/g). The superior capacitance was ascribed to the increased MXene surface area and fast ion diffusion.

Easy restacking between delaminated MXene sheets is inevitable during the fabrication process because of the strong Van der Waals forces and hydrogen bond interactions between the interlayers, which hinders the accessibility to electrolyte ions and limits the full utilization of active sites. To tackle this issue, one efficient strategy has been extensively investigated for increasing the space between MXene layers by introducing additive interlayer spacers. Carbon materials (such as graphene and carbon nanotubes) have both good conductivity and large lateral size/length, which can significantly expand the layer spacing and enhance the capacitance of MXene-based supercapacitors without sacrificing conductivity and energy density. Zhao et al. [97] incorporated MXene with 0D onion-like carbon (OLC), 1D CNTs, and 2D graphene to fabricate a novel sandwich structure, respectively, and then directly used the composite film as an electrode for flexible supercapacitors. When 1 mol/L MgSO_4 solution was used as the electrolyte, the volumetric capacitance of pristine $\text{Ti}_3\text{C}_2\text{T}_x$ film was 360 F/cm³ at 2 mV/s. When the scan rate reaches 200 mV/s, the capacitance of pristine $\text{Ti}_3\text{C}_2\text{T}_x$ was only 162 F/cm³, while those of the sandwich structure $\text{Ti}_3\text{C}_2\text{T}_x$ composite films were 218 F/cm³, 280 F/cm³, and 320 F/cm³, respectively. Moreover, the rate performance of these hybrid films was further improved compared with that of pristine $\text{Ti}_3\text{C}_2\text{T}_x$ films, which is attributed to the enhanced electrical conductivities of the sandwich-like structures. However, the inherent low capacitance of carbon materials partially restrains

the further enhancement of the overall capacitance of the MXene films. Similarly, to further incorporate interlayer spacers with high specific capacitance and conductivity, Yu et al. [123] combined two kinds of 2D olefinic materials by introducing antimonene to hybridize with MXene, which simultaneously approached the state-of-the-art capacitance and excellent flexibility. The introduction of antimonene into freestanding MXene films could expand the spacing between MXene layers in MXene-based electrodes and maintain the original flexibility, thus realized a remarkable areal capacitance of 3403 mF/cm^2 in $1 \text{ mol/L H}_2\text{SO}_4$. The excellent energy storage performance of antimonene/MXene films was attributed to the synergistic effect between $\text{Ti}_3\text{C}_2\text{T}_x$ and antimonene. First, the ordered layer-by-layer inner structure in the hybrid films could increase the electron diffusion at the interfaces. Second, both $\text{Ti}_3\text{C}_2\text{T}_x$ and antimonene are highly active pseudocapacitive materials, whose interstratified molecular-level coupling optimized the charge transfer between the two species. Additionally, various studies have revealed that different cations (such as Al^{3+} , Li^+ , NH_4^+ , Mg^{2+} , Na^+ , and K^+) can chemically or electrochemically intercalate into MXenes layers, which can increase the layer spacing in varying degrees and improve the volume volumetric capacitance [44, 118, 124]. For example, Lukatskaya et al. [118] reported that the intercalation of a variety of cations with various charges and sizes between MXene layers could significantly improve the capacitance of $\text{Ti}_3\text{C}_2\text{T}_x$ MXene electrode films prepared from the multilayer $\text{Ti}_3\text{C}_2\text{T}_x$ powder. To obtain the cation intercalated electrode films, the $\text{Ti}_3\text{C}_2\text{T}_x$ flakes were treated by being dispersed in various aqueous solutions (acid, alkali, salt), respectively, and subsequently filtered on a polyester membrane. Benefiting from the increased spacing and accessibility, the $\text{Ti}_3\text{C}_2\text{T}_x$ paper electrodes manifested intercalation-induced high capacitances and decreased resistance.

The support-free MXene films, even MXene/inorganic additive composite films, possess relatively high flexibility and capacitance; however, they still face serious problems in achieving flexible devices, mainly because of the small lateral size and high stiffnesses of the MXene nanosheets [125]. Taking the advantages of the flexible structure of polymer chains and excellent adhesion of MXene/polymer composite membranes, molecular-level coupling between MXene sheets and macromolecules can be achieved by intercalating polymers into MXene sheets, which provides a new option and is considered to have immense potential for the fabrication of MXene-based composite films in flexible supercapacitor with excellent electrochemical performance. These polymer-insert agents suppress the restacking of MXene sheets and remarkably enhance the flexibility and ion transport rate of MXene/polymer composite membranes. For example, Wang et al. [110] fabricated an extremely flexible polymer/MXene hybrid

film with engineering 3D ion transport channels (Fig. 13a), which exhibited attractive electrochemical capacitance and excellent mechanical strength. Bacterial cellulose (BC) was chosen as the substrate for loading MXene because of its ultra-fine interconnected nanofiber network, excellent water retention performance, and high tensile strength [126, 127], which enables the high mechanical strength and faster electron transport in the microchannels. The MXene/BC composite electrode with MXene loading of 5 mg/cm^2 showed ultra-high capacitance of 2084 mF/cm^2 at 3 mA/cm^2 and 1304 mF/cm^2 at 50 mA/cm^2 (Fig. 13b, c), high deformation (bendable, and even foldable), and excellent mechanical strength (three times greater than that of pristine MXene electrodes). The honeycomb-like architecture formed by interconnected MXene sheets in the film had a high capacitance, which accelerated contacts between electrolyte ions and redox-active sites and reduced the ion transport pathway. MXene/polymer composite membranes with conductive polymers are also widely investigated because of the excellent conductivity and increased mechanical properties. $\text{Ti}_3\text{C}_2\text{T}_x$ /polypyrrole (PPy) and $\text{Ti}_3\text{C}_2\text{T}_x$ /polyaniline (PANI) films have been successfully fabricated via VAF, and their electrochemical performance was systematically investigated [128, 129]. The composite films exhibited enhanced cycling stability and higher pseudocapacitive charge storage than a neat MXene membrane. In addition to fabricating composite membranes with polymers or other additions, novel asymmetric supercapacitors with pristine MXene membranes and conductive polymers as the anode and cathode, respectively, have also been developed. Boota and Gogotsi [130] reported an organic-inorganic asymmetric device in which $\text{Ti}_3\text{C}_2\text{T}_x$ MXene serves as a general pseudocapacitive anode material for a range of conductive polymer (CP)-containing cathodes [PANI, PPy, and poly(3,4-ethylenedioxythiophene) (PEDOT)] (Fig. 13d). The materials with different chemical properties electrochemically complement each other in a device, which create an expanded voltage window of up to 1.45 V and excellent cycling performance in $3 \text{ mol/L H}_2\text{SO}_4$ solution. The shape of the CVs in these asymmetric devices is similar to a pair of distinct redox peaks before and after 20,000 cycles, among which the PANI-containing devices showed a high capacitance retention (nearly 88%) (Fig. 13e). Subsequently, Li et al. [12] designed a flexible asymmetric pseudocapacitor, in which a wavy $\text{Ti}_3\text{C}_2\text{T}_x$ MXene film was used as a negative electrode and a compact rGO/CNT/PANI was used as a positive electrode. In this work, polystyrene (PS) spheres were used as a template to fabricate 3D porous $\text{Ti}_3\text{C}_2\text{T}_x$ films, which were then further transformed into flexible and freestanding wavy $\text{Ti}_3\text{C}_2\text{T}_x$ films by mechanical compression under 10 MPa . The wavy MXene films exhibited an enhanced volumetric capacitance of 1277 F/cm^3

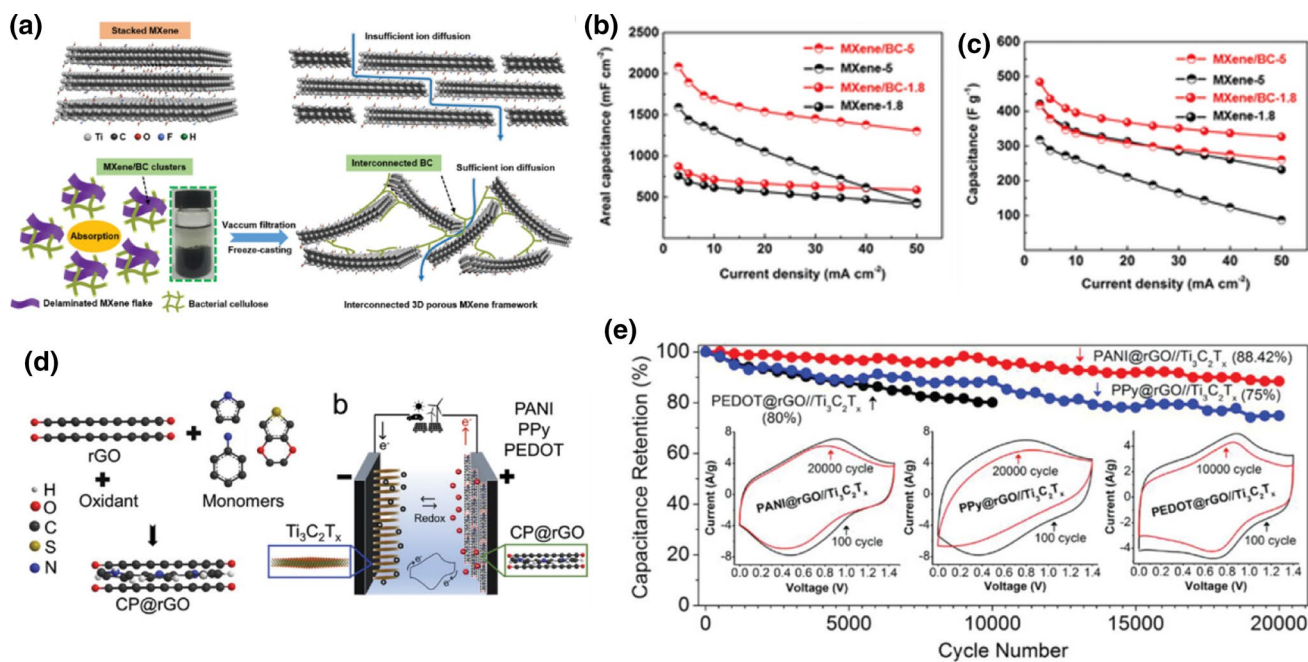


Fig. 13 **a** Schematic of fabricating the porous $\text{Ti}_3\text{C}_2\text{T}_x$ architecture. **b** Areal capacitance and **c** gravimetric capacitance of MXene/BC films and pristine MXene electrodes with MXene loading 1.8 mg/cm^2 and 5 mg/cm^2 . Reproduced with permission [110]. Copyright 2019, Wiley-VCH. **d** Fabrication process of organic–inorganic asymmet-

ric devices. **e** Cycle life performance of the optimized compositions. Insets in **e** are the CV curves before and after long cycling of the devices. Reproduced with permission [130]. Copyright 2019, Wiley-VCH

and 89% capacitance retention rate at 1000 mV/s because of the facilitated ion transport and highly compact structure. More importantly, the solid-state device fabricated with $\text{PVA}/\text{H}_2\text{SO}_4$ gel electrolyte delivered a maximum volumetric energy density of 63.5 $\text{W}\cdot\text{h}/\text{L}$ and a maximum volumetric power density of 34.3 kW/L , greater than the reported $\text{Ti}_3\text{C}_2\text{T}_x/\text{rGO}$ quasi solid-state asymmetric device (11.1 $\text{W}\cdot\text{h}/\text{L}$, 18 kW/L) [131].

These MXene-based films produce supercapacitors with high specific capacitance, enhanced energy, and enhanced power density. Moreover, the excellent flexibility and outstanding mechanical properties promote the development of flexible supercapacitors, which are promising to meet the rigid requirements for powering wearable electronics. Although various types of MXenes have been successfully synthesized, most studied MXene films applied to supercapacitors are mainly based on a few kinds of MXene materials (such as Ti_3C_2 and $\text{Mo}_{1.33}\text{C}$). Therefore, vast efforts should be devoted to exploring the feasibility of novel MXenes with different transition metal atoms in supercapacitors. In addition, the electrochemical performance of MXene-based films can be enhanced via subsequent processing, including surface treatment, internal structure engineering, and the combination of other MXene flakes with various additives, even novel synthesis methods and integrated design of supercapacitors.

Batteries

Batteries are currently one of the most widely used electrochemical power sources applied in mobile devices. Tremendous efforts have been devoted to the performance improvement of Li–S batteries, Li-ion batteries (LIBs), and Na-ion batteries. Although batteries have great importance and are extensively used in practical applications, some intrinsic properties cause deficiencies as well, such as the shuttle effect of soluble Li_2S_x in Li–S batteries, slow Li^+ transport rate, and poor redox reaction dynamics in LIBs. Importantly, with the rapid development of green batteries and the pursuit of small, light, thin, and flexible batteries, MXene-based electrodes (mainly involving MXene membranes in this paper) are expected to realize these goals for its lower Li diffusion barrier (0.07 eV), abundant surface redox reaction, and superior electrical conductivity. In Li–S batteries, the insulative effect of elemental sulfur, the shuttle effect of soluble Li_2S_x , and the volume expansion of sulfur during charging and discharging processes lead to poor cycling performance of Li–S batteries and low utilization of active materials, which severely restrict their development and practical application [132, 133]. Regarding the issue above, Tang et al. [109] fabricated a highly flexible $\text{Ti}_3\text{C}_2\text{T}_x$ conductive film using a VAF method and evenly fixed amorphous S on the surface of $\text{Ti}_3\text{C}_2\text{T}_x$ flakes by physical vapor deposition

(Fig. 14a). The $\text{Ti}_3\text{C}_2\text{T}_x/\text{S}$ conductive paper demonstrated the similar flexibility to pristine $\text{Ti}_3\text{C}_2\text{T}_x$ films, whose fracture stress, fracture strain, and conductivity were up to 79.6 MPa, 1.8%, and 1650 S/cm, respectively (Fig. 14b, c). Importantly, the film delivered a high capacity (1383 mA·h/g at 0.1 C) and an ultralow capacity decay rate (0.014% after 1500 cycles). To reveal the mechanisms behind the excellent cycling performance, XPS analysis was used to investigate the surface chemistry of various samples and the growth kinetics of the sulfate complex layer. Lithium polysulfides (LiPSs) physically confined on the surface of polar MXene flakes will further interact with oxygen-containing functional groups and exposed Ti atoms, which will lead to the formation of a thiosulfate thin layer and further react with LiPSs to form a sulfate. With these reactions, the thickness of the sulfate gradually accumulates during the cycles, and an effective sulfate complex layer is formed to function as a protective membrane. This membrane is beneficial

for inhibiting the LiPSs shuttle effect and then reasonably increasing the cycling performance.

MXene, part of the growing 2D family, with good conductivity and short Li^+ diffusion paths, has been directed toward Li^+ battery applications. Various studies demonstrate that the surface morphology of MXenes greatly affects the performance of LIBs. DFT computations on the Ti_3C_2 monolayer with bare, fluorinated, and hydroxylated surfaces showed that the electronic properties were strongly associated with the surface terminations. Specifically, the bare Ti_3C_2 monolayer presents a low barrier for Li^+ diffusion and delivers high Li storage capacity, while $-\text{F}$ and $-\text{OH}$ functionalized surfaces block Li transport and decrease the Li storage capacity. This computational investigation demonstrated the potential of MXene-based films for Li-ion battery anodes [134]. Similar to the above DFT computations, Yan et al. [135] employed first-principles calculations to investigate the influence of $-\text{S}/-\text{O}$

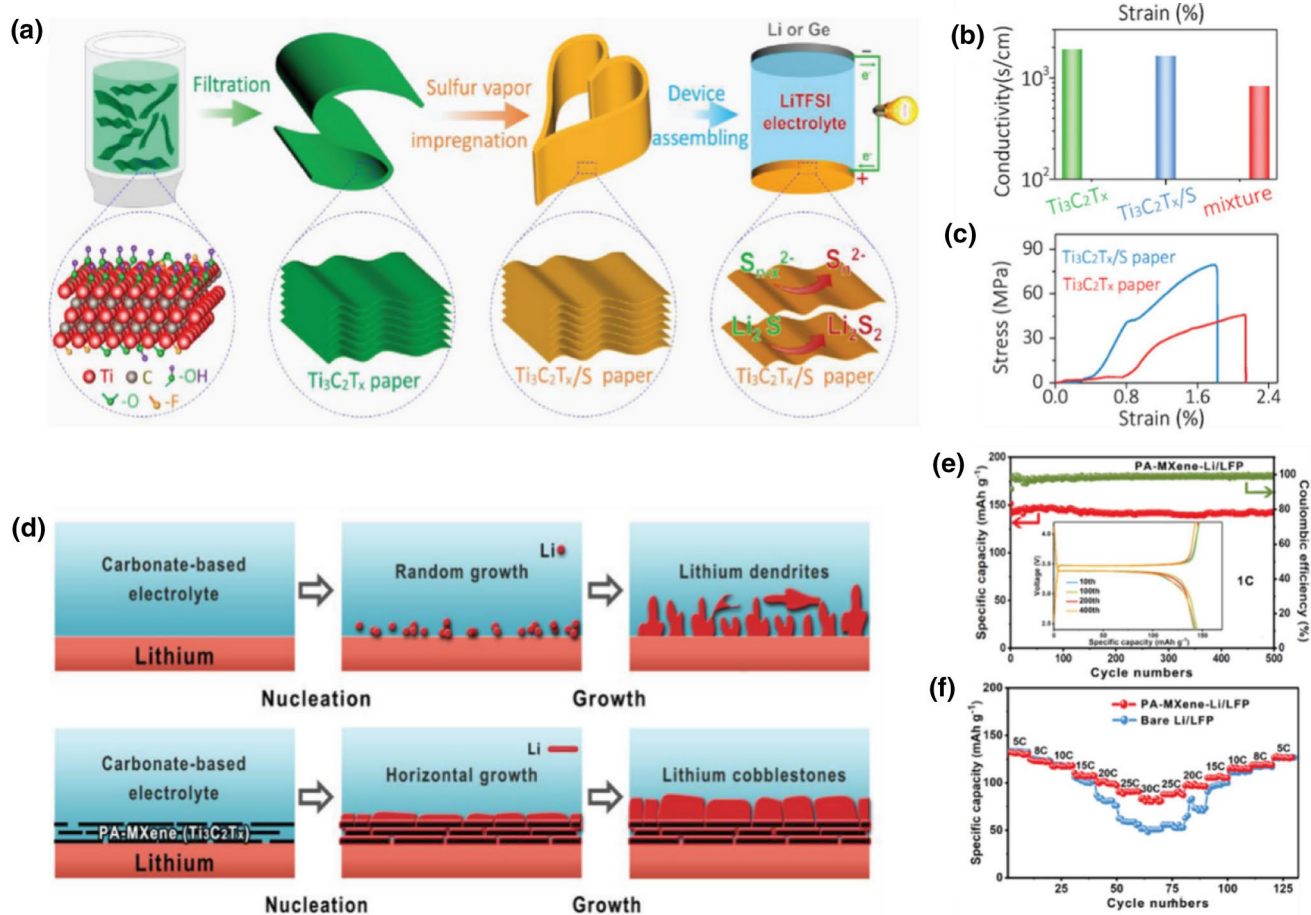


Fig. 14 **a** Schematic of the $\text{Ti}_3\text{C}_2\text{T}_x/\text{S}$ composite paper. **b** Electronic conductivity and **c** stress-strain curve of pristine $\text{Ti}_3\text{C}_2\text{T}_x$ paper, $\text{Ti}_3\text{C}_2\text{T}_x/\text{S}$ paper, and $\text{Ti}_3\text{C}_2\text{T}_x$ -S mixture electrodes. Reproduced with permission [109]. Copyright 2019, Wiley-VCH. **d** Schematic of lithium plating on bare lithium and parallelly aligned MXene (PA-MXene) layers. **e** Cycling performance and Coulombic efficiency

of a PA-MXene-Li/LiFePO₄ full cell. Inset in **e** is the charging and discharging profiles of the cell from 10 to 400 cycles. **f** Rate performance of PA-MXene-Li/LiFePO₄ and Li/LiFePO₄ cells at different rates ranging from 5 to 30 C. Reproduced with permission [138]. Copyright 2019, Wiley-VCH

terminations on the structural properties and lithium storage capacity of V_2C MXene. The feasibility of V_2CT_2 as a LIB anode is assessed by the Li^+ adsorption abilities of the functionalized 2D materials. Simulation results showed $-O/-S$ terminated V_2C exhibited a lower Li^+ diffusion barrier and a larger Li^+ capacity than $-F/-OH$ terminated V_2CT_x , which favors the potential for alternative anodes. Note that various works have taken advantage of the abundance of functional groups on the surface of MXenes, and various MXene-based films were successfully fabricated that exhibited excellent lithium-ion storage capacity and a long cycle life in LIB applications. As revealed by Wei et al. [136], terminated functional groups (such as $-O$, $-OH$, and $-F$) on the surface of MXene and liquid metal (3 °C GaInSnZn) can easily react with oxygen to form a thin oxide layer on the surface, which can facilitate the practical adhesion between MXene paper and liquid metal. On the basis of the flexible nature of MXene paper and excellent fluidity of liquid metal, a lightweight, flexible and freestanding MXene/liquid metal paper was fabricated as an anode for LIBs, in which liquid metal was confined in the matrix of MXene paper. Given the high electrical conductivity (2500 S/cm) and excellent wettability (36.4°) between liquid metal and MXene paper, this flexible composite paper exhibited significantly increased energy density (507.42 mA·h/g at 50 mA/g) in batteries without binders or conductive additive. Chen et al. [137] reported a Ti_3C_2 /PEDOT hybrid membrane with excellent lithium-ion-storage performance because of the synergistic effect of the increased interlayer spacing and facilitated interface redox processes. Tested in lithium-ion half cells, the Ti_3C_2 /PEDOT electrode showed enhanced reversible capacity (~ 300 mA·h/g) and increased cycle stability compared with both pristine Ti_3C_2 membrane and neat PEDOT electrodes. After 100 cycles, the capacity of the Ti_3C_2 /PEDOT electrode maintained 255 mA·h/g while pristine Ti_3C_2 and conventionally synthesized PEDOT remained only 195 and 237 mA·h/g, respectively. The enhanced capacity is ascribed to the fast electrolyte diffusion and the synergistic effect originating from the surface redox processes between PEDOT and Ti_3C_2 layers. Yang et al. [138] also demonstrated that the parallelly aligned MXene sheets could effectively induce the nucleation and growth of lithium metal on its surface, producing dendrite-free metal anodes for metal ion batteries (Fig. 14d). These parallelly aligned MXene thin films were fabricated via a facile self-assembly procedure at a water/air interface. The hybrid films were then fabricated by a simple roll-to-roll method and used as an anode in lithium metal batteries. The hybrid anodes possessed a long life up to 900 h at 1 mA·h/cm² and 400 h even at excellent deep stripping–plating capacities up to 35 mA·h/cm². To further examine the real practicability, a full cell with $LiFePO_4$

(LTP) as a cathode was constructed, which presented high stability up to 500 cycles with a capacity of 140 mA·h/g at 1 C (1 C = 172 mA·h/g) and 83.5 mA·h/g even at 30 C (Fig. 14e, f). The excellent electrochemical performance is ascribed to the large amount of fluorine terminations on the MXene surfaces, which can form a uniform and dense solid electrolyte interface with LiF and effectively optimize the electromigration of lithium ions.

Sodium-ion batteries are another essential energy storage device because of their security and low-cost. In addition, Ti_3C_2 sheets with $-F$, $-O$, and $-OH$ terminations are approximately 0.19, 0.2 and 0.013 eV on Na^+ diffusion barriers, respectively, demonstrating superior Na^+ diffusion kinetics and great application potential in sodium-ion batteries [139]. Zhao et al. [140] synthesized molecular-level coupling PDDA-BP/ Ti_3C_2 heterostructures via an electrostatic attraction self-assembly strategy, which play to the advantages of the high capacity of black phosphorene (BP) and excellent electronic conductivity of Ti_3C_2 . The freestanding films exhibited an ultra-high reversible capacity (1112 mA·h/g) after 500 cycles and showed excellent cycling stability. In addition, DFT calculations were performed to reveal the underlying mechanism of the sodiation and relaxation process when adding Na on top of the surface functional groups (such as $-F$, $-O$, and $-OH$). The simulation results manifest that the enhanced sodium storage performance and resultant ultra-high reversible capacity may be ascribed to the fast ion diffusion and charge transfer kinetics originating from the mixed absorption and decreased binding energy. By processing the various 2D MXene flakes (V_2CT_x , $Ti_3C_2T_x$, and Mo_2CT_x) onto hollow spheres (PMMA), respectively, and further forming 3D architectures via a sacrificial template approach, freestanding, flexible, and highly conductive 3D macroporous MXene films were successfully fabricated [141]. The 3D MXene films manifested enhanced Na-ion storage capacity and improved reversible capacities (295, 310, and 290 mA·h/g at 2.5 C obtained by 3D $Ti_3C_2T_x$, V_2CT_x , and Mo_2CT_x films, respectively). After 1000 cycles at 2.5 C, the hybrid films exhibited higher capacity retention (53.8%, 55.3%, and 51.2% retained by 3D $Ti_3C_2T_x$, V_2CT_x , and Mo_2CT_x films, respectively) than those previously reported for the $Ti_3C_2T_x$ /CNT film electrode ($\approx 40\%$) [142]. The enhancement of Coulombic efficiency is ascribed to the partial removal of surface terminations on MXene surfaces via thermal annealing during the preparation process, and another contribution was attributed to the optimized surface chemistry of MXenes.

Gas and Liquid Separations

Gas Separation

A MXene membrane assembled from MXene sheets has regular interlayer transport channels and abundant surface terminal groups to assist gas separation, which can effectively screen and separate various gas molecules. Sheet-on-sheet stacked MXene membranes with aligned and regular

sub-nanometer channels have been successfully applied to the separation of H₂ and CO₂ (Fig. 15a). The freestanding MXene membranes were fabricated on an AAO support via VAF method. The 2D laminated structure allows hydrogen to pass freely between the sheets while larger gas molecules are selectively rejected, which causes excellent gas separation performance with H₂ permeability > 2200 Barrer and H₂/CO₂ selectivity > 160, as shown in Fig. 15b. The better permeability and selectivity of MXene membranes are

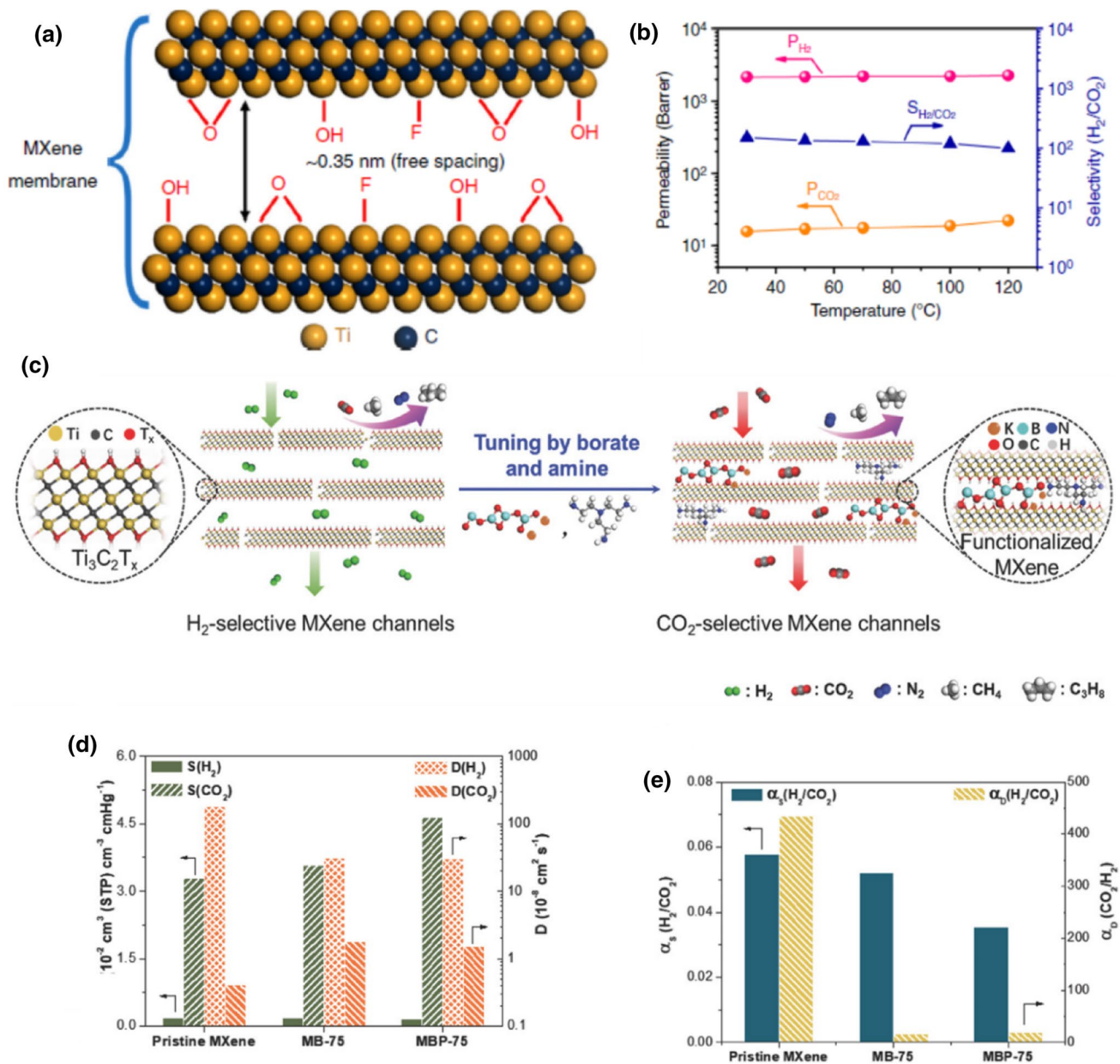


Fig. 15 **a** Schematic of the free space between adjacent MXene flakes in the membrane. **b** Separation performance for H₂/CO₂ in 2-μm-thick MXene membrane. Reproduced with permission [70]. Copyright 2018, Nature Publishing Group. **c** Schematic of the MXene films for H₂-selectivity and CO₂-selectivity. **d** Solubility (S) and dif-

fusivity (D) of MXene-based films for H₂ and CO₂. **e** Sorption selectivity (α_s) and diffusion selectivity (α_D) for H₂/CO₂ in different MXene-based nanofilms. Reproduced with permission [68]. Copyright 2018, Wiley-VCH

related to their chemical composition and structure, which is superior to other separation membranes using physical capture such as a graphene membrane [147]. Molecular dynamic simulations were performed to study the transfer process to better illustrate the gas separation mechanism. These models were largely consistent with experiments, which indicated molecular sieving occurred during the gas diffusion process [70].

Shen et al. [68] reported the design and engineering of the MXene membrane for efficiently separating H_2/CO_2 (Fig. 15c), which has highly tunable transport channels and ultrathin thickness. The CO_2 solubility and CO_2/H_2 sorption selectivity of MXene nanofilms modified with polyethylenimine (PEI) and borate were greatly improved (Fig. 15d, e). Interestingly, borate and PEI-functionalized MXene laminates showed tunable interlayer spacing and preferential CO_2 selective penetration over H_2 while the CO_2/H_2 permeation selectivity is only 1.4 because of the lower diffusivity originating from CO_2 being larger than H_2 .

Liquid Separation

MXenes provide new sight into developing advanced liquid separation membranes because of the desirable properties for ion separation in an aqueous solution, such as the abundant terminations on the surface, hydrophilic nature, and sufficiently large specific area. The assembled MXene membranes possess extremely short transport pathways and abundant nanochannels. Moreover, the transport channels between MXene layers can be tuned by the type of inserted ions/organic molecules and the size of flakes [148]. Therefore, MXene membranes have attracted attention in water purification and have been proved to possess extraordinary permeation properties. Ren et al. [149] pioneered the use of MXene membranes to realize charge- and size-selective rejection of ions and molecules, studying the correlation between water flux and membrane thickness. The micrometer-thick $Ti_3C_2T_x$ membranes possessed ultrafast water permeation ($37.4 L/(bar h m^2)$) as well as attractive separation property toward single-, double-, triple-charged metal cations and dye cations with varying sizes. The ions with radii larger than the interlayer distance demonstrated a low permeation rate ($\sim 7 \times 10^{-4} mol/(hm^2)$) because they did not pass through the $Ti_3C_2T_x$ membrane. Moreover, by electrically modulating the surface charge of $Ti_3C_2T_x$ with an applied voltage (electrochemical filtration), the ion sieving process can be further enhanced. In addition, Wang et al. [67] successfully prepared a 2D lamellar membrane with ultrashort transport pathways and abundant nanochannels using simple filtration. The positively charged $Fe(OH)_3$ colloidal solution was used as a pore former to create expanded channels through intercalating layers of negatively charged MXene flakes. This MXene membrane could reject particles

with a diameter larger than 2.5 nm in water (> 90%) and still maintain high water permeation and excellent stability (more than $1000 L/(m^2 hbar)$) after continuously operating for 24 h. Subsequently, an Al^{3+} intercalated and non-swelling MXene membrane was prepared via a simple “concentration diffusion” method. Al^{3+} played a crucial role in firmly fixing the MXene layers through the interaction with oxygen-containing terminal groups on the MXene surfaces and provided Al^{3+} -intercalated MXene membranes an opportunity to withstand the high driving force induced in a high salt concentration. Compared with pristine MXene membranes without any treatment, the Al^{3+} -intercalated MXene membrane effectively inhibited the swelling in the aqueous solution. The ion-intercalated membrane showed both a high salt rejection rate (NaCl, 99.5%) and improved water flux ($2.81 L/(m^2 h)$) [150].

Additionally, Xie et al. [151] reported a novel 2D MXene-based separation membrane for removing multiple kinds of charged heavy metal ions (HMIs) from water without pressure. The microchannel structure of the membrane was optimized through the intercalation of rGO flakes between MXene layers. Furthermore, the effect of $Ti_3C_2T_x$ terminal groups on the favorable surface interactions between HMIs and $Ti_3C_2T_x$ was studied by DFT calculations. The results showed that the charge transfer in the most stable configurations could drive the reductive removal of $HCrO_4^-$ via the enhancement of $HCrO_4^-$ absorption.

Electromagnetic Interference Shielding

The role of EMI shielding is to cut off the propagation of electromagnetic waves to eliminate interference. Shielding is a basic and effective way to solve the problem of electromagnetic interference. The main function or mechanism of EMI shielding materials is to reflect electromagnetic radiations by charge carriers that interact directly with the electromagnetic field [152]. Good EMI shielding materials should exhibit excellent performance in two aspects: reduce partial harmful electromagnetic radiations and protect internal devices from external radiations [153–155]. Therefore, the entire surface of the electromagnetic shielding device must be continuously conductive, and the absorption of electromagnetic radiations must occur through the material's electric and/or magnetic dipoles interaction with radiations. In addition, a thin, lightweight, and easy-to-fabricate MXene films enable superior EMI shielding performance, which indicate great potential in the fields of flexible wearable electronic devices and aerospace [156].

Shahzad et al. [157] demonstrated that flexible MXene films ($Ti_3C_2T_x$, $Mo_2TiC_2T_x$, and $Mo_2Ti_2C_3T_x$) and nacre-like MXene–sodium alginate composite films have potential applications in EMI shielding. The EMI shielding effect (EMI SE) of $Ti_3C_2T_x$ film with a thickness of $45 \mu m$ was up

to 92 dB (Fig. 16b) because of the high electrical conductivity of the $\text{Ti}_3\text{C}_2\text{T}_x$ films and the multiple internal reflections between the $\text{Ti}_3\text{C}_2\text{T}_x$ interlayers. Shahzad et al. [157] proposed a mechanism to explain the high-performance of EMI SE (Fig. 16a): MXene will reflect the wave as soon as the incident electromagnetic wave (green arrows) strikes the MXene surface. Abundant charge carriers on the highly conductive surfaces of MXene will reflect part of the electromagnetic wave into the environment (light blue arrows). Part of the electromagnetic wave passing through the MXene structure will be absorbed by the induced local dipole resulting from the termination groups. Based on the same mechanism, incident waves with lower energy will also undergo a similar process when they encounter the next MXene sheets, resulting in multiple internal reflections to absorb more incident waves (dashed black arrows). Each time the electromagnetic waves pass through MXene sheets during transmission, their intensity will decrease sharply, which can attenuate or even eliminate EM waves. A comparison with materials previously studied for EMI SE clearly indicates that MXene and MXene-based composites had the best EMI SE, which were superior to most materials, including graphene [158–160], carbon nanotubes [161], iron oxide [162, 163], polymer-based foams [164], iron-aluminum–silicon alloy [165], and polymer composites with metal base filler [166].

Recently, a $\text{Ti}_3\text{C}_2\text{T}_x$ /cellulose nanofibers (CNFs) composite paper with a nacre-like structure was successfully

achieved with dual strengthening and toughening mechanisms [83]. The abundant active terminal groups on the layered $\text{Ti}_3\text{C}_2\text{T}_x$ surfaces interact with CNFs through hydrogen bonds to compensate for the lack of mechanical properties of MXenes [28]. Through the interaction between 1D CNFs and 2D $\text{Ti}_3\text{C}_2\text{T}_x$, the $\text{Ti}_3\text{C}_2\text{T}_x$ /CNF composite paper exhibited high tensile strength (up to 135.4 MPa) and fracture strain (up to 16.7%) (Fig. 16d). In addition, $\text{Ti}_3\text{C}_2\text{T}_x$ /CNF composite paper possessed high conductivity (up to 739.4 S/m) and excellent electromagnetic shielding efficiency while maintaining an ultrathin thickness (minimum thickness 47 μm). The EMI mechanism was shown in Fig. 16c. The EMI SE of the $\text{Ti}_3\text{C}_2\text{T}_x$ /CNF composite films with 80 wt% of $\text{Ti}_3\text{C}_2\text{T}_x$ reached 25.8 dB at 12.4 GHz (Fig. 16e), which fully meets the commercial shielding requirements. Furthermore, Cao et al. [167] constructed an ultrathin and flexible carbon nanotubes/MXene/cellulose (CMC) nanofibrils composite paper with gradient and ‘sandwich structure’ via facile alternate VAF strategy and explored the effect of the proportion of different components and internal structures on the EMI SE. The ternary composite paper demonstrated a high electrical conductivity of 2506.6 S/m and an enhanced EMI SE of 38.4 dB, which is better than the randomly assembled CMC mixture composite paper (23.4 dB) and pure MXene films (34 dB). In addition to the excellent EMI SE, the composite paper also exhibits an improved mechanical property with a tensile strength of 94.9 ± 7.4 MPa and outstanding toughness

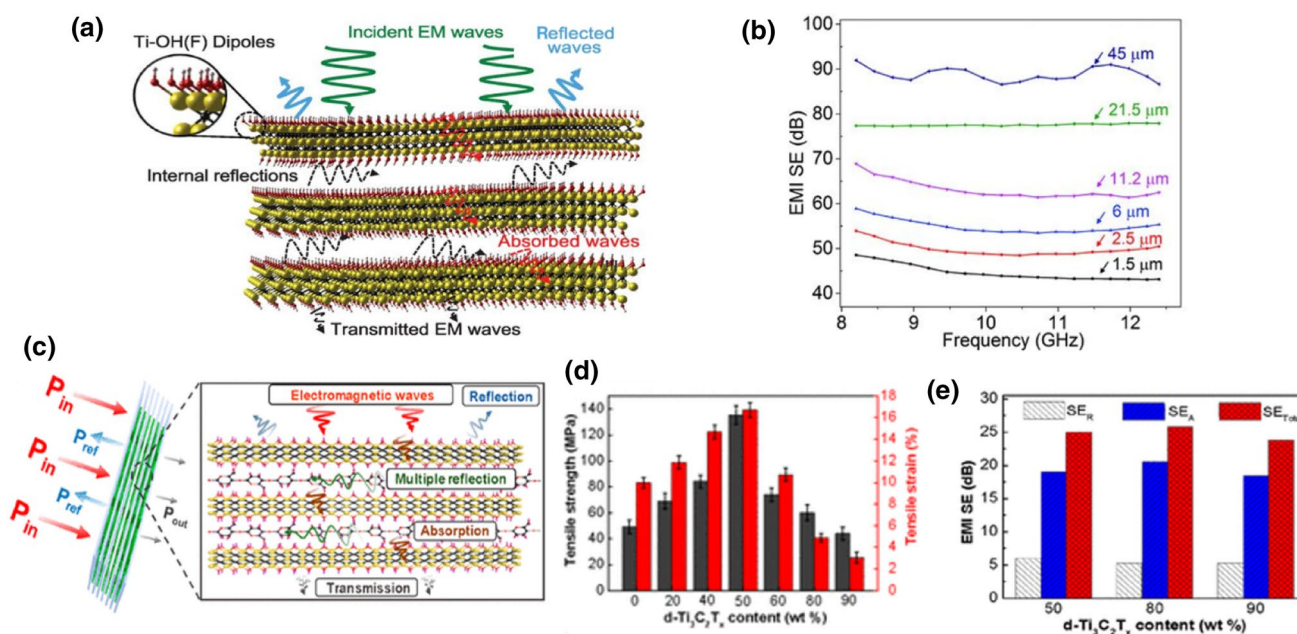


Fig. 16 a Proposed EMI shielding process. b EMI SE of $\text{Ti}_3\text{C}_2\text{T}_x$ film at different thicknesses. Reproduced with permission [157]. Copyright 2016, American Association for the Advancement of Science. c Schematic of the EMI shielding process in the $\text{Ti}_3\text{C}_2\text{T}_x$ /CNF composite paper. d Tensile strength and tensile strain of the $d\text{-Ti}_3\text{C}_2\text{T}_x$ /

CNF composite paper with different $\text{Ti}_3\text{C}_2\text{T}_x$ contents. e Comparison of total EMI shielding effectiveness, microwave absorption (SEA), and microwave reflection (SER) at 12.4 GHz of the $d\text{-Ti}_3\text{C}_2\text{T}_x$ /CNF composite paper with different $d\text{-Ti}_3\text{C}_2\text{T}_x$ contents. Reproduced with permission [83]. Copyright 2018, American Chemical Society

(2.1 MJ/m³), which can meet the requirements for practical application in EMI shielding materials, especially in the field of wearable or portable electronic devices.

Other Applications

The unique structures and properties of MXene-based films indicate their potential for other applications such as catalysis [168] and sensors [169]. For example, the application of MXene-based films as electrocatalysts toward superior oxygen evolution reactions (OER) has been reported. Ma et al. [168] hybridized graphitic carbon nitrides (g-C₃N₄) with Ti₃C₂ sheets to assemble a robust freestanding film, which showed efficient and cost-effective electrocatalysts activity for OER. Hierarchical pores and a highly hydrophilic surface contribute greatly to its excellent performance. The former provides a high double-layer capacitance and catalytically active surface area. The latter is favorable for aqueous electrolytes in electrochemical devices, which smooths the pathway for electrolyte ions approaching active sites.

MXenes also exhibit excellent antibacterial effect [170]. Ti₃C₂T_x has a high antibacterial activity against both *Escherichia coli* and *Bacillus subtilis*. After 4 h of exposure to 200 µg/mL³ Ti₃C₂T_x, more than 98% of the bacteria lost their activity. The antibacterial mechanism of MXenes is ascribed to the anionic nature of its surface and oxygen-containing terminations on which bonding to a lipopolysaccharide string of the cell membrane through hydrogen bond can prevent bacterial contamination by inhibiting nutrient uptake [171]. Jastrzebska et al. [172] found that Ti₃C₂ had an inhibitory effect on *E. coli* while Ti₂C did not. Combined with the XPS analysis of the two materials, the antibacterial effect of MXene was considered to be related to its specific molecular structure. Rasool et al. [80] applied Ti₃C₂T_x sheets for water purification and studied the antibacterial activity of these Ti₃C₂T_x modified membranes. These micrometer-thick Ti₃C₂T_x membranes were fabricated via filtration on a polyvinylidene fluoride (PVDF) substrate, demonstrating excellent antibacterial activity against Gram-negative and Gram-positive bacteria. In addition, they compared the antibacterial rate of fresh and aged Ti₃C₂T_x MXene membranes. The former showed more than 73% inhibition against *B. subtilis* and 67% against *E. coli*, while the latter manifested over 99% growth inhibition of both bacteria under the same conditions. The enhanced antibacterial activity of the aged membrane is ascribed to the synergistic effect between the Ti₃C₂T_x nanosheets and TiO₂/C formed by surface oxidation.

Interestingly, MXenes have excellent photothermal conversion property, which involves a straightforward and highly efficient energy conversion process. The pioneering work was proposed by Wang's group, who were inspired by the excellent electromagnetic wave absorption of MXene and subsequent heat generation process [173]. In this study,

MXene sheets exfoliated by a general HF etching method were further assembled with PVDF membrane to form a self-floating thin membrane. The barrier exhibited a high light-to-water evaporation efficiency of 84% and nearly 100% light-to-heat conversion efficiency under 1 sunlight illumination (1 kW/m²). Given the outstanding photothermal behavior and salt rejection rate, a hydrophobic/hydrophilic double-layer evaporation structure was also designed for solar desalination [174]. The upper layer is porous, hydrophobic, and light-absorbing MXene membrane modified with trimethoxy(1H,1H,2H,2H-perfluorodecyl) silane (PFDTMS), which can realize photothermal conversion, vapor evaporation, and salt-blocking. The lower layer is a piece of commercial filter membrane for stable water supply. The membrane can further be assembled into a whole solar steam generation device with commercial polystyrene foam, which can act as a thermal insulator and floater (Fig. 17a). The heat is localized on a hydrophobic Ti₃C₂ membrane to avoid directly heating water, thus leading to the quickly rising temperature on the membrane surface (an increase to ~39 °C in 10 min) because of the non-wettable upper layer. Based on this structure, the hydrophobic membrane with 10 mg Ti₃C₂ loading mass can manifest a stable water evaporation rate of 1.31 kg/(m² h) and the corresponding solar steam conversion efficiency up to 71% under only one sun. Given the high salt reject rate, the solar steam generation device delivers extraordinary stability (continuous running over 200 h) with little salt attaching to the membrane surface. Similarly, a Janus, vertically aligned Ti₃C₂ MXene aerogel with hydrophobic upper layer and hydrophilic bottom layer was engineered for salt resistance in the solar desalination process (Fig. 17b) [175].

Given that MXene films and their composite films possess peculiar physical (metallic conductivity, layered structure), chemical (abundant surface groups), and biological properties (hydrophilicity), some parameters associated with these properties may occur subtle deviation as external conditions changes. Therefore, MXene-based films can also work as sensors to detect the change of external conditions [34]. Various sensing platforms based on MXenes have been fabricated to quantitatively detect external stimuli, including pressures, ion/gases, sounds, and human activities. Stacking properties between MXene flakes can be altered by external strain changes, which in turn can change the interflake resistance of the devices. Therefore, this property can also be utilized to fabricate highly sensitive MXene-based piezoresistive sensors for detecting slight movements of humans. An et al. [176] illustrated that Ti₃C₂/PDAC films could be used as a strain sensor, which can sense object deformations according to the resistance change during the deformation process. Compared with traditional graphene- or carbon nanotube-based sensors for electronic devices, the Ti₃C₂/PDAC membrane-based sensor was more suitable for

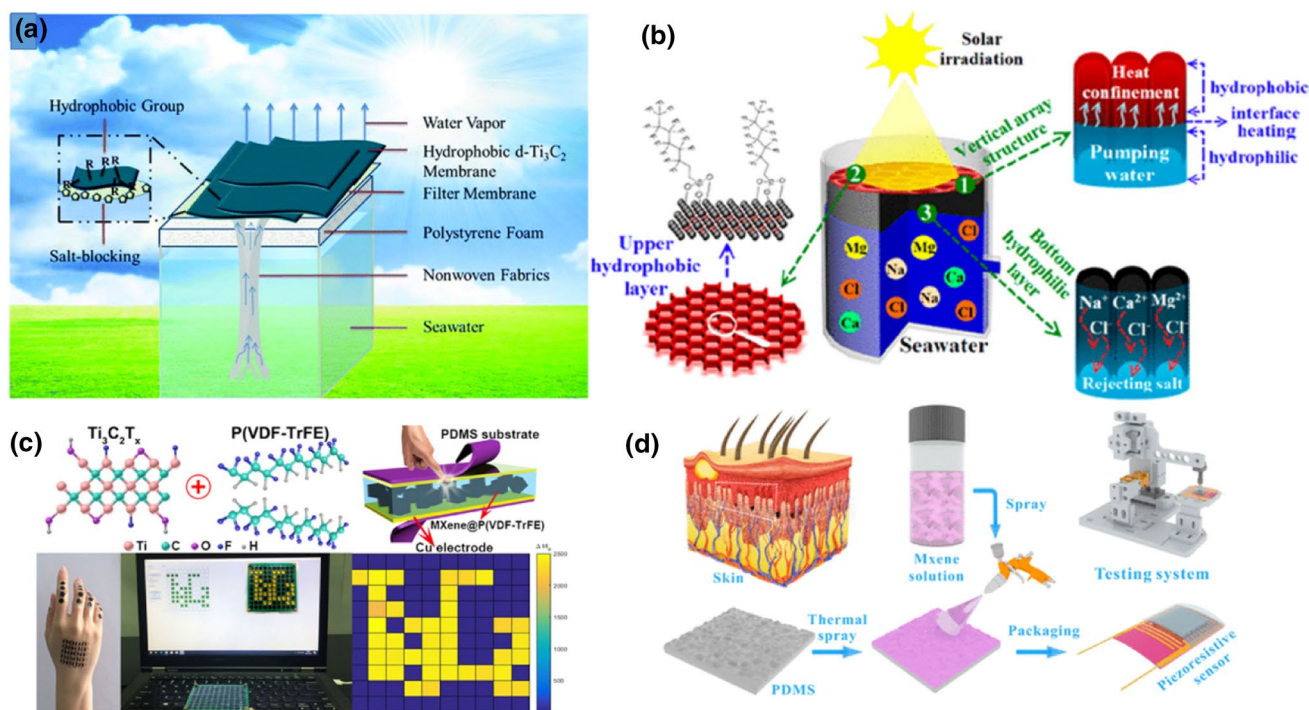


Fig. 17 **a** Schematic of a solar desalination device based on a hydrophobic Ti₃C₂T_x membrane. Reproduced with permission [174]. Copyright 2018, Royal Society of Chemistry. **b** Vertically aligned Janus MXene aerogels for solar desalination. Reproduced with permission [175]. Copyright 2019, American Chemical Society. **c** Schematic of a flexible pressure sensor (10 mm×8 mm) and the correspond-

ing pressure mapping profiles of the pixel signals. Reproduced with permission [177]. Copyright 2020, American Chemical Society. **d** Design and assembly of piezoresistive sensors with bionic spinous microstructure. Reproduced with permission [178]. Copyright 2020, American Chemical Society

a variety of complex deformation modes while maintaining outstanding electronic conductivity. Li et al. [177] prepared hydrophobic organic/inorganic composite films using natural poly(vinylidene fluoride) trifluoroethylene (P(VDF-TrFE)) and multilayer Ti₃C₂T_x via a spin-coating method, and then fabricated stable piezoresistive pressure sensors (Fig. 17c). In addition, a MXene-based piezoresistive sensor with a randomly distributed spinous microstructure was reported that was designed and manufactured by a facile abrasive paper stencil printing process. This sensor was ultrathin, flexible, and highly sensitive, and therefore easy to attach to the skin for detecting human activities and human–computer interaction (Fig. 17d) [178]. MXenes films can also be utilized for detecting various gases and biologically important molecule because of the active surface functional groups and layered structures. Ti₃C₂T_x chemical sensors with superior sensing properties for volatile organic compounds (VOCs) (ammonia, acetone, ethanol, and propanol) in ultralow detection limits (50–100 ppb) have been synthesized [179]. This sensor manifested high selectivity toward hydrogen-bonding gases over acidic gases. Moreover, given the Ti₃C₂T_x is fully covered with active surface terminations, selectivity toward various gases may also be adjusted by ligand functionalization or defect control. For example, Ti₃C₂T_x sensors via

surface treatment with fluoroalkylsilane (FOTS) molecules provide a superhydrophobic surface, mechanical/environmental stability, and enhanced sensing performance for oxygen-containing VOCs (acetone, ethanol, and 2-propanol) [180].

MXene-based films are promising alternatives to traditional 2D films widely used in application fields mentioned above because of the various functionalities of MXenes. While the emerging MXene nanomaterials are promising in the design of performance films, numerous challenges still restrict the commercialization of current MXene-film based devices. For example, MXene-based films are not cost-competitive and are difficult to scale-up despite the improved performances compared with commercial devices. Improved etching methods and novel assemblies can be used to further investigate and solve these problems. Additionally, a reasonable design of MXene-film based devices should be further explored and promoted, especially in energy-storage devices and flexible electronics. The relationship between property and structure in the MXene-based films need to be further investigated by theoretical simulation and experiment, which is an important step for in-depth research of the nature of MXenes to broaden their application fields.

Conclusion and Outlook

In summary, we focused on the synthesis methods, assembly technologies, and intriguing applications of MXene-based films. The practical applications of MXene films have been summarized in detail, including electrochemical energy storage, EMI shielding, membrane separation, and other emerging applications. MXene sheets and composite films have gained remarkable achievements in various applications. Nevertheless, the development of MXene film is still in its infancy, and there are still many urgent problems that remain to be addressed before the practical application of these materials.

Even if the synthesis of various MXenes is feasible by theoretical calculation, the practical fabrication is still limited by the difficulty of synthesizing the corresponding MAX phases and instability of MXenes after exfoliation. Therefore, new exfoliation and synthesis methods of new precursors are urgent problem. Green and mild synthetic approaches are necessary for fabricating MXenes with high yield and high quality. Additionally, we can devote vast attention to the new-style MAX phases with various elements (not only conventional Al) to expand the MAX family.

Similar to other 2D nanomaterials, morphological improvements and surface modifications have a significant impact on increasing the number of active sites. This is very important for the production of high quality MXenes with large-scale sheets and nano-scale defects for application to high-performance batteries or capacitors. For lithium-ion batteries and sodium-ion batteries, if the electrode material has no defects or functional groups, it will greatly reduce the initial Coulombic efficiency. In addition, a higher specific surface area and pore volume can be effectively produced by controlling the porosity and curvature of the MXene layer; the addition of specific groups has a promoting effect on both aspects.

Although MXenes have achieved outstanding performance in many applications, especially in the field of electrochemistry, their physical mechanisms need to be further studied. The restacking tendency of MXene sheets may not be satisfactory in realizing its actual electrochemical performance, which can result in adverse effects on the commercial production of MXene-film based devices. For example, when MXene film is fabricated by a simpler VAF method, if the nanosheets are self-stacking, the electrochemical performance will decrease from the reduced transmission of ions. Therefore, an in-depth study of the restacking mechanism is necessary. In addition, the combination of a hydrophilic surface and excellent electrical conductivity enables multifunctional design and excellent processing performance of MXenes, which provides new

opportunities for exploring unknown fields and introduce a new pathway to the advancement in various applications. Another promising prospect is to convert MXene to commercial products [181]. To meet the requirements of industrial application, the technical issues for mass production and process integration should be considered. Therefore, it is necessary to well understand the exfoliation mechanism of the MAX phase from the most basic structure and investigate the mechanism of the fundamental properties and functionality of MXenes to scale-up the production process in a low-cost and environmentally friendly way.

Acknowledgements This work was supported by the National Natural Science Foundation of China (21878062), the Natural Science Foundation of Heilongjiang Province for Distinguished Young Scholars (JQ2020B001) and State Key Laboratory of Urban Water Resource and Environment (Harbin Institute of Technology) (No. 2020DX02).

Open Access This article is licensed under a Creative Commons Attribution 4.0 International License, which permits use, sharing, adaptation, distribution and reproduction in any medium or format, as long as you give appropriate credit to the original author(s) and the source, provide a link to the Creative Commons licence, and indicate if changes were made. The images or other third party material in this article are included in the article's Creative Commons licence, unless indicated otherwise in a credit line to the material. If material is not included in the article's Creative Commons licence and your intended use is not permitted by statutory regulation or exceeds the permitted use, you will need to obtain permission directly from the copyright holder. To view a copy of this licence, visit <http://creativecommons.org/licenses/by/4.0/>.

References

1. Novoselov KS, Geim AK, Morozov SV et al (2004) Electric field effect in atomically thin carbon films. *Science* 306(5696):666–669
2. Peng L, Ye S, Song J et al (2019) Solution-phase synthesis of few-layer hexagonal antimonene nanosheets via anisotropic growth. *Angew Chem Int Ed Engl* 58(29):9891–9896. <https://doi.org/10.1002/anie.201900802>
3. Wang X, He JJ, Zhou BQ et al (2018) Bandgap-tunable preparation of smooth and large two-dimensional antimonene. *Angew Chem Int Ed Engl* 57(28):8668–8673
4. Ren XH, Zhou J, Qi X et al (2017) Few-layer black phosphorus nanosheets as electrocatalysts for highly efficient oxygen evolution reaction. *Adv Energy Mater* 7(19):1700396. <https://doi.org/10.1002/aenm.201700396>
5. Chen H, Yang ZZ, Zhang ZH et al (2019) Construction of a nanoporous highly crystalline hexagonal boron nitride from an amorphous precursor for catalytic dehydrogenation. *Angew Chem Int Ed Engl* 58(31):10626–10630. <https://doi.org/10.1002/anie.201904996>
6. Manzeli S, Ovchinnikov D, Pasquier D et al (2017) 2D transition metal dichalcogenides. *Nat Rev Mater* 2:17033
7. Xiao X, Song HB, Lin SZ et al (2016) Scalable salt-templated synthesis of two-dimensional transition metal oxides. *Nat Commun* 7:11296
8. Lv L, Yang ZX, Chen K et al (2019) 2D layered double hydroxides for oxygen evolution reaction: from fundamental design

- to application. *Adv Energy Mater* 9(17):1803358. <https://doi.org/10.1002/aenm.201803358>
9. Zhao SJ, Kang W, Xue JM (2015) MXene nanoribbons. *J Mater Chem C* 3(4):879–888. <https://doi.org/10.1039/c4tc01721h>
 10. Tang J, Mathis TS, Kurra N et al (2019) Tuning the electrochemical performance of titanium carbide MXene by controllable *in situ* anodic oxidation. *Angew Chem Int Ed Engl* 58(49):17849–17855. <https://doi.org/10.1002/anie.201911604>
 11. VahidMohammadi A, Mojtavavi M, Caffrey NM et al (2019) Assembling 2D MXenes into highly stable pseudocapacitive electrodes with high power and energy densities. *Adv Mater* 31(8):e1806931. <https://doi.org/10.1002/adma.201806931>
 12. Li K, Wang XH, Wang XF et al (2020) All-pseudocapacitive asymmetric MXene-carbon-conducting polymer supercapacitors. *Nano Energy* 75:104971. <https://doi.org/10.1016/j.nanoen.2020.104971>
 13. Li XL, Hao JN, Liu R et al (2020) Interfacing MXene flakes on fiber fabric as an ultrafast electron transport layer for high performance textile electrodes. *Energy Storage Mater* 33:62–70. <https://doi.org/10.1016/j.ensm.2020.05.004>
 14. Naguib M, Mochalin VN, Barsoum MW et al (2014) 25th anniversary article: MXenes new family of two-dimensional materials. *Adv Mater* 26(7):992–1005. <https://doi.org/10.1002/adma.201304138>
 15. Naguib M, Mashtalir O, Carle J et al (2012) Two-dimensional transition metal carbides. *ACS Nano* 6(2):1322–1331
 16. Naguib M, Halim J, Lu J et al (2013) New two-dimensional niobium and vanadium carbides as promising materials for Li-ion batteries. *J Am Chem Soc* 135(43):15966–15969. <https://doi.org/10.1021/ja405735d>
 17. Ghidui M, Naguib M, Shi C et al (2014) Synthesis and characterization of two-dimensional Nb₄C₃ (MXene). *Chem Commun* 50(67):9517–9520. <https://doi.org/10.1039/c4cc03366c>
 18. Urbankowski P, Anasori B, Makaryan T et al (2016) Synthesis of two-dimensional titanium nitride Ti₄N₃ (MXene). *Nanoscale* 8(22):11385–11391
 19. Halim J, Kota S, Lukatskaya MR et al (2016) Synthesis and characterization of 2D molybdenum carbide (MXene). *Adv Funct Mater* 26(18):3118–3127. <https://doi.org/10.1002/adfm.201505328>
 20. Li M, Lu J, Luo K et al (2019) Element replacement approach by reaction with Lewis acidic molten salts to synthesize nanolaminated MAX phases and MXenes. *J Am Chem Soc* 141(11):4730–4737
 21. Khazaei M, Arai M, Sasaki T et al (2013) Novel electronic and magnetic properties of two-dimensional transition metal carbides and nitrides. *Adv Funct Mater* 23(17):2185–2192. <https://doi.org/10.1002/adfm.201202502>
 22. Tang X, Guo X, Wu WJ et al (2018) 2D metal carbides and nitrides (MXenes) as high-performance electrode materials for lithium-based batteries. *Adv Energy Mater* 8(33):1801897. <https://doi.org/10.1002/aenm.201801897>
 23. Naguib M, Kurtoglu M, Presser V et al (2011) Two-dimensional nanocrystals produced by exfoliation of Ti₃AlC₂. *Adv Mater* 23(37):4248–4253
 24. Enyashin AN, Ivanovskii AL (2012) Atomic structure, comparative stability and electronic properties of hydroxylated Ti₂C and Ti₃C₂ nanotubes. *Comput Theor Chem* 989:27–32. <https://doi.org/10.1016/j.comptc.2012.02.034>
 25. Fashandi H, Ivády V, Eklund P et al (2015) Dirac points with giant spin-orbit splitting in the electronic structure of two-dimensional transition-metal carbides. *Phys Rev B* 92(15):155142. <https://doi.org/10.1103/physrevb.92.155142>
 26. Yang PH, Chao DL, Zhu CR et al (2016) Ultrafast-charging supercapacitors based on corn-like titanium nitride nanostructures. *Adv Sci* 3(6):1500299
 27. Xie Y, Naguib M, Mochalin VN et al (2014) Role of surface structure on Li-ion energy storage capacity of two-dimensional transition-metal carbides. *J Am Chem Soc* 136(17):6385–6394
 28. Gao LF, Li C, Huang WC et al (2020) MXene/polymer membranes: synthesis, properties, and emerging applications. *Chem Mater* 32(5):1703–1747. <https://doi.org/10.1021/acs.chemmater.9b04408>
 29. Dhanabalan SC, Ponraj JS, Guo Z et al (2017) Emerging trends in phosphorene fabrication towards next generation devices. *Adv Sci* 4(6):1600305
 30. Pei JJ, Gai X, Yang J et al (2016) Producing air-stable monolayers of phosphorene and their defect engineering. *Nat Commun* 7:10450
 31. Ghidui M, Lukatskaya MR, Zhao MQ et al (2014) Conductive two-dimensional titanium carbide ‘clay’ with high volumetric capacitance. *Nature* 516(7529):78–81
 32. Wang LB, Zhang H, Wang B et al (2016) Synthesis and electrochemical performance of Ti₃C₂T_x with hydrothermal process. *Electron Mater Lett* 12(5):702–710. <https://doi.org/10.1007/s13391-016-6088-z>
 33. Xu C, Wang LB, Liu ZB et al (2015) Large-area high-quality 2D ultrathin Mo₂C superconducting crystals. *Nat Mater* 14(11):1135–1141
 34. Yang Q, Wang YK, Li XL et al (2018) Recent progress of MXene-based nanomaterials in flexible energy storage and electronic devices. *Energy Environ Mater* 1(4):183–195. <https://doi.org/10.1002/eem2.12023>
 35. Guo YT, Jin S, Wang LB et al (2020) Synthesis of two-dimensional carbide Mo₂CT_x MXene by hydrothermal etching with fluorides and its thermal stability. *Ceram Int* 46(11):19550–19556. <https://doi.org/10.1016/j.ceramint.2020.05.008>
 36. Xie XH, Xue Y, Li L et al (2014) Surface Al leached Ti₃AlC₂ as a substitute for carbon for use as a catalyst support in a harsh corrosive electrochemical system. *Nanoscale* 6(19):11035–11040
 37. Li TF, Yao LL, Liu QL et al (2018) Fluorine-free synthesis of high-purity Ti₃C₂T_x (T=OH, O) via alkali treatment. *Angew Chem Int Ed Engl* 57(21):6115–6119
 38. Yasaei P, Tu Q, Xu YB et al (2019) Mapping hot spots at heterogeneities of few-layer Ti₃C₂ MXene sheets. *ACS Nano* 13(3):3301–3309
 39. Lin H, Wang YW, Gao SS et al (2018) Theranostic 2D tantalum carbide (MXene). *Adv Mater* 30(4):1703284. <https://doi.org/10.1002/adma.201703284>
 40. Wang J, Tang J, Ding B et al (2017) Hierarchical porous carbons with layer-by-layer motif architectures from confined soft-template self-assembly in layered materials. *Nat Commun* 8:15717
 41. Ran JR, Gao GP, Li FT et al (2017) Ti₃C₂ MXene co-catalyst on metal sulfide photo-absorbers for enhanced visible-light photocatalytic hydrogen production. *Nat Commun* 8:13907
 42. Tian W, VahidMohammadi A, Reid MS et al (2019) Multifunctional nanocomposites with high strength and capacitance using 2D MXene and 1D nanocellulose. *Adv Mater* 31(41):e1902977
 43. Xu BZ, Zhu MS, Zhang WC et al (2016) Ultrathin MXene-micropattern-based field-effect transistor for probing neural activity. *Adv Mater* 28(17):3333–3339
 44. Anasori B, Lukatskaya MR, Gogotsi Y (2017) 2D metal carbides and nitrides (MXenes) for energy storage. *Nat Rev Mater* 2(2):1–17. <https://doi.org/10.1038/natrevmats.2016.98>
 45. Natu V, Pai R, Sokol M et al (2020) 2D Ti₃C₂T_x MXene synthesized by water-free etching of Ti₃AlC₂ in polar organic solvents. *Chem* 6(3):616–630. <https://doi.org/10.1016/j.chempr.2020.01.019>
 46. Lipatov A, Alhabeb M, Lukatskaya MR et al (2016) Effect of synthesis on quality, electronic properties and environmental stability of individual monolayer Ti₃C₂ MXene flakes. *Adv Electron Mater* 2(12):1600255. <https://doi.org/10.1002/aeml.201600255>

47. Maleski K, Ren CE, Zhao MQ et al (2018) Size-dependent physical and electrochemical properties of two-dimensional MXene flakes. *ACS Appl Mater Interfaces* 10(29):24491–24498. <https://doi.org/10.1021/acsami.8b04662>
48. Halim J, Lukatskaya MR, Cook KM et al (2014) Transparent conductive two-dimensional titanium carbide epitaxial thin films. *Chem Mater* 26(7):2374–2381
49. Zhao XF, Vashisth A, Pohn E et al (2019) Antioxidants unlock shelf-stable $Ti_3C_2T_x$ (MXene) nanosheet dispersions. *Matter* 1(2):513–526. <https://doi.org/10.1016/j.matt.2019.05.020>
50. Zhao XF, Radovic M, Green MJ (2020) Synthesizing MXene nanosheets by water-free etching. *Chem* 6(3):544–546. <https://doi.org/10.1016/j.chempr.2020.02.013>
51. Fashandi H, Dahlqvist M, Lu J et al (2017) Synthesis of Ti_3AuC_2 , $Ti_3Au_2C_2$ and Ti_3IrC_2 by noble metal substitution reaction in Ti_3SiC_2 for high-temperature-stable Ohmic contacts to SiC. *Nat Mater* 16(8):814–818
52. Li YB, Shao H, Lin ZF et al (2020) A general Lewis acidic etching route for preparing MXenes with enhanced electrochemical performance in non-aqueous electrolyte. *Nat Mater* 19(8):894–899
53. Naguib M, Presser V, Tallman D et al (2011) On the topotactic transformation of Ti_2AlC into a Ti–C–O–F cubic phase by heating in molten lithium fluoride in air. *J Am Ceram Soc* 94(12):4556–4561. <https://doi.org/10.1111/j.1551-2916.2011.04896.x>
54. Zhou J, Zha X, Chen FY et al (2016) A two-dimensional zirconium carbide by selective etching of Al_3C_3 from nanolaminated $Zr_3Al_3C_5$. *Angew Chem Int Ed Engl* 55(16):5008–5013
55. Zhou YC, He LF, Lin ZJ et al (2013) Synthesis and structure–property relationships of a new family of layered carbides in Zr–Al(Si)–C and Hf–Al(Si)–C systems. *J Eur Ceram Soc* 33(15–16):2831–2865
56. Zhou J, Zha XH, Zhou XB et al (2017) Synthesis and electrochemical properties of two-dimensional hafnium carbide. *ACS Nano* 11(4):3841–3850
57. Pang SY, Wong YT, Yuan S et al (2019) Universal strategy for HF-free facile and rapid synthesis of two-dimensional MXenes as multifunctional energy materials. *J Am Chem Soc* 141(24):9610–9616
58. Nicolosi V, Chhowalla M, Kanatzidis MG et al (2013) Liquid exfoliation of layered materials. *Science* 340(6139):1226419. <https://doi.org/10.1126/science.1226419>
59. Hu T, Hu MM, Li ZJ et al (2016) Interlayer coupling in two-dimensional titanium carbide MXenes. *Phys Chem Chem Phys* 18(30):20256–20260
60. Mashtalir O, Naguib M, Mochalin VN et al (2013) Intercalation and delamination of layered carbides and carbonitrides. *Nat Commun* 4:1716
61. Naguib M, Unocic RR, Armstrong BL et al (2015) Large-scale delamination of multi-layers transition metal carbides and carbonitrides “MXenes.” *Dalton Trans* 44(20):9353–9358
62. Eames C, Islam MS (2014) Ion intercalation into two-dimensional transition-metal carbides: global screening for new high-capacity battery materials. *J Am Chem Soc* 136(46):16270–16276. <https://doi.org/10.1021/ja508154e>
63. Maleski K, Mochalin VN, Gogotsi Y (2017) Dispersions of two-dimensional titanium carbide MXene in organic solvents. *Chem Mater* 29(4):1632–1640. <https://doi.org/10.1021/acs.chemmater.6b04830>
64. Mashtalir O, Lukatskaya MR, Zhao MQ et al (2015) Amine-assisted delamination of Nb₂C MXene for Li-ion energy storage devices. *Adv Mater* 27(23):3501–3506
65. Shang TX, Lin ZF, Qi CS et al (2019) 3D macroscopic architectures from self-assembled MXene hydrogels. *Adv Funct Mater* 29(33):1903960. <https://doi.org/10.1002/adfm.201903960>
66. Deng YQ, Shang TX, Wu ZT et al (2019) Fast gelation of $Ti_3C_2T_x$ MXene initiated by metal ions. *Adv Mater* 31(43):1902432. <https://doi.org/10.1002/adma.201902432>
67. Ding L, Wei Y, Wang Y et al (2017) A two-dimensional lamellar membrane: MXene nanosheet stacks. *Angew Chem Int Ed Engl* 56(7):1825–1829
68. Shen J, Liu GZ, Ji YF et al (2018) 2D MXene nanofilms with tunable gas transport channels. *Adv Funct Mater* 28(31):1801511. <https://doi.org/10.1002/adfm.201801511>
69. Zhang F, Guo X, Xiong P et al (2020) Interface engineering of MXene composite separator for high-performance Li–Se and Na–Se batteries. *Adv Energy Mater* 10(20):2000446. <https://doi.org/10.1002/aenm.202000446>
70. Ding L, Wei Y, Li L et al (2018) MXene molecular sieving membranes for highly efficient gas separation. *Nat Commun* 9(1):155
71. Bao WZ, Liu L, Wang CY et al (2018) Facile synthesis of crumpled nitrogen-doped MXene nanosheets as a new sulfur host for lithium-sulfur batteries. *Adv Energy Mater* 8(13):1702485. <https://doi.org/10.1002/aenm.201702485>
72. Luo JQ, Zhao S, Zhang HB et al (2019) Flexible, stretchable and electrically conductive MXene/natural rubber nanocomposite films for efficient electromagnetic interference shielding. *Compos Sci Technol* 182:107754. <https://doi.org/10.1016/j.compscitech.2019.107754>
73. Wang HR, Li L, Zhu CC et al (2019) *In situ* polymerized $Ti_3C_2T_x$ /PDA electrode with superior areal capacitance for supercapacitors. *J Alloys Compd* 778:858–865. <https://doi.org/10.1016/j.jallcom.2018.11.172>
74. Shen L, Zhou XY, Zhang XL et al (2018) Carbon-intercalated $Ti_3C_2T_x$ MXene for high-performance electrochemical energy storage. *J Mater Chem A* 6(46):23513–23520. <https://doi.org/10.1039/C8TA09600G>
75. Zhao X, Wang Z, Dong J et al (2020) Annealing modification of MXene films with mechanically strong structures and high electrochemical performance for supercapacitor applications. *J Power Sources* 470:228356. <https://doi.org/10.1016/j.jpowsour.2020.228356>
76. Zhao WW, Peng JL, Wang WK et al (2019) Interlayer hydrogen-bonded metal porphyrin frameworks/MXene hybrid film with high capacitance for flexible all-solid-state supercapacitors. *Small* 15(18):1901351. <https://doi.org/10.1002/smll.201901351>
77. Ling Z, Ren CE, Zhao MQ et al (2014) Flexible and conductive MXene films and nanocomposites with high capacitance. *PNAS* 111(47):16676–16681
78. Podsiađo P, Kaushik AK, Arruda EM et al (2007) Ultrastrong and stiff layered polymer nanocomposites. *Science* 318(5847):80–83. <https://doi.org/10.1126/science.1143176>
79. Lu XH, Yu MH, Wang GM et al (2014) Flexible solid-state supercapacitors: design, fabrication and applications. *Energy Environ Sci* 7(7):2160–2181. <https://doi.org/10.1039/C4EE00960F>
80. Rasool K, Mahmoud KA, Johnson DJ et al (2017) Efficient antibacterial membrane based on two-dimensional $Ti_3C_2T_x$ (MXene) nanosheets. *Sci Rep* 7(1):1598
81. Tang H, Li WL, Pan LM et al (2018) *In situ* formed protective barrier enabled by sulfur@titanium carbide (MXene) ink for achieving high-capacity, long lifetime Li-S batteries. *Adv Sci* 5(9):1800502
82. Liang X, Rangom Y, Kwok CY et al (2017) Interwoven MXene nanosheet/carbon-nanotube composites as Li-S cathode hosts. *Adv Mater* 29(3):1603040. <https://doi.org/10.1002/adma.201603040>
83. Cao WT, Chen FF, Zhu YJ et al (2018) Binary strengthening and toughening of MXene/cellulose nanofiber composite paper with nacre-inspired structure and superior electromagnetic

- interference shielding properties. *ACS Nano* 12(5):4583–4593. <https://doi.org/10.1021/acsnano.8b00997>
84. Lipomi DJ, Tee BCK, Vosgueritchian M et al (2011) Stretchable organic solar cells. *Adv Mater* 23(15):1771–1775. <https://doi.org/10.1002/adma.201004426>
85. Huang HC, He JQ, Wang ZX et al (2020) Scalable, and low-cost treating-cutting-coating manufacture platform for MXene-based on-chip micro-supercapacitors. *Nano Energy* 69:104431. <https://doi.org/10.1016/j.nanoen.2019.104431>
86. Montazeri K, Currie M, Verger L et al (2019) Beyond gold: spin-coated Ti_3C_2 -based MXene photodetectors. *Adv Mater* 31(43):e1903271
87. Zhang CJ, Anasori B, Seral-Ascaso A et al (2017) Transparent, flexible, and conductive 2D titanium carbide (MXene) films with high volumetric capacitance. *Adv Mater* 29(36):1702678. <https://doi.org/10.1002/adma.201702678>
88. Dillon AD, Ghidui MJ, Krick AL et al (2016) Highly conductive optical quality solution-processed films of 2D titanium carbide. *Adv Funct Mater* 26(23):4162–4168. <https://doi.org/10.1002/adfm.201600357>
89. Hsia B, Marschewski J, Wang S et al (2014) Highly flexible, all solid-state micro-supercapacitors from vertically aligned carbon nanotubes. *Nanotechnology* 25(5):055401
90. Hantanasirisakul K, Alhabeb M, Lipatov A et al (2019) Effects of synthesis and processing on optoelectronic properties of titanium carbonitride MXene. *Chem Mater* 31(8):2941–2951. <https://doi.org/10.1021/acs.chemmater.9b00401>
91. Wang K, Zhou YF, Xu WT et al (2016) Fabrication and thermal stability of two-dimensional carbide Ti_3C_2 nanosheets. *Ceram Int* 42(7):8419–8424. <https://doi.org/10.1016/j.ceramint.2016.02.059>
92. Sheng XX, Zhao YF, Zhang L et al (2019) Properties of two-dimensional Ti_3C_2 MXene/thermoplastic polyurethane nanocomposites with effective reinforcement via melt blending. *Compos Sci Technol* 181:107710. <https://doi.org/10.1016/j.compscitech.2019.107710>
93. Yan J, Ren CE, Maleski K et al (2017) Flexible MXene/graphene films for ultrafast supercapacitors with outstanding volumetric capacitance. *Adv Funct Mater* 27(30):1701264. <https://doi.org/10.1002/adfm.201701264>
94. Kim SJ, Choi J, Maleski K et al (2019) Interfacial assembly of ultrathin, functional MXene films. *ACS Appl Mater Interfaces* 11(35):32320–32327
95. Yan LL, Yang XB, Long J et al (2020) Universal unilateral electro-spinning/spraying strategy to construct water-unidirectional *Janus* membranes with well-tuned hierarchical micro/nanostructures. *Chem Commun (Camb)* 56(3):478–481
96. Jiang CM, Wu C, Li XJ et al (2019) All-electrospun flexible triboelectric nanogenerator based on metallic MXene nanosheets. *Nano Energy* 59:268–276. <https://doi.org/10.1016/j.nanoen.2019.02.052>
97. Zhao MQ, Ren CE, Ling Z et al (2015) Flexible MXene/carbon nanotube composite paper with high volumetric capacitance. *Adv Mater* 27(2):339–345. <https://doi.org/10.1002/adma.201404140>
98. Cui Y, Xie X, Yang R et al (2019) Cold pressing-built microreactors to thermally manipulate microstructure of MXene film as an anode for high-performance lithium-ion batteries. *Electrochim Acta* 305:11–23. <https://doi.org/10.1016/j.electacta.2019.02.085>
99. Xu SK, Wei GD, Li JZ et al (2017) Binder-free $Ti_3C_2T_x$ MXene electrode film for supercapacitor produced by electrophoretic deposition method. *Chem Eng J* 317:1026–1036. <https://doi.org/10.1016/j.cej.2017.02.144>
100. Qin LQ, Tao QZ, Liu XJ et al (2019) Polymer-MXene composite films formed by MXene-facilitated electrochemical polymerization for flexible solid-state microsupercapacitors. *Nano Energy* 60:734–742. <https://doi.org/10.1016/j.nanoen.2019.04.002>
101. Bai J, Zhao BC, Lin S et al (2020) Construction of hierarchical V_4C_3 -MXene/ MoS_2 /C nanohybrids for high rate lithium-ion batteries. *Nanoscale* 12(2):1144–1154
102. Fan ZM, Wang YS, Xie ZM et al (2018) A nanoporous MXene film enables flexible supercapacitors with high energy storage. *Nanoscale* 10(20):9642–9652
103. Orangi J, Beidaghi M (2020) A review of the effects of electrode fabrication and assembly processes on the structure and electrochemical performance of 2D MXenes. *Adv Funct Mater* 30(47):2005305. <https://doi.org/10.1002/adfm.202005305>
104. Hart JL, Hantanasirisakul K, Lang AC et al (2019) Control of MXenes' electronic properties through termination and intercalation. *Nat Commun* 10(1):522
105. Zhou J, Yu JL, Shi LD et al (2018) A conductive and highly deformable all-pseudocapacitive composite paper as supercapacitor electrode with improved a real and volumetric capacitance. *Small* 14(51):1803786. <https://doi.org/10.1002/smll.201803786>
106. Zheng LX, Guan LT, Song JL et al (2019) Rational design of a sandwiched structure $Ni(OH)_2$ nanohybrid sustained by amino-functionalized graphene quantum dots for outstanding capacitance. *Appl Surf Sci* 480:727–737. <https://doi.org/10.1016/j.apsusc.2019.02.243>
107. Zhao YL, Han CH, Yang JW et al (2015) Stable alkali metal ion intercalation compounds as optimized metal oxide nanowire cathodes for lithium batteries. *Nano Lett* 15(3):2180–2185. <https://doi.org/10.1021/acs.nanolett.5b00284>
108. Yan CS, Fang ZW, Lv C et al (2018) Significantly improving lithium-ion transport via conjugated anion intercalation in inorganic layered hosts. *ACS Nano* 12(8):8670–8677
109. Tang H, Li WL, Pan LM et al (2019) A robust, freestanding MXene-sulfur conductive paper for long-lifetime Li-S batteries. *Adv Funct Mater* 29(30):1901907. <https://doi.org/10.1002/adfm.201901907>
110. Wang YM, Wang X, Li XL et al (2019) Engineering 3D ion transport channels for flexible MXene films with superior capacitive performance. *Adv Funct Mater* 29(14):1900326. <https://doi.org/10.1002/adfm.201900326>
111. Qin LQ, Jiang JX, Tao QZ et al (2020) A flexible semitransparent photovoltaic supercapacitor based on water-processed MXene electrodes. *J Mater Chem A* 8(11):5467–5475. <https://doi.org/10.1039/D0TA00687D>
112. Zhang CJ, Kremer MP, Seral-Ascaso A et al (2018) Stamping of flexible, coplanar micro-supercapacitors using MXene inks. *Adv Funct Mater* 28(9):1705506. <https://doi.org/10.1002/adfm.201705506>
113. Zhao Q, Zhu QZ, Miao JW et al (2019) 2D MXene nanosheets enable small-sulfur electrodes to be flexible for lithium-sulfur batteries. *Nanoscale* 11(17):8442–8448
114. Hu MM, Hu T, Li ZJ et al (2018) Surface functional groups and interlayer water determine the electrochemical capacitance of $Ti_3C_2T_x$ MXene. *ACS Nano* 12(4):3578–3586
115. Fan ZM, Wang YS, Xie ZM et al (2018) Modified MXene/holey graphene films for advanced supercapacitor electrodes with superior energy storage. *Adv Sci (Weinh)* 5(10):1800750
116. Guo ZL, Zhou J, Si C et al (2015) Flexible two-dimensional $Ti_{n+1}C_n$ ($n = 1, 2$ and 3) and their functionalized MXenes predicted by density functional theories. *Phys Chem Chem Phys* 17(23):15348–15354
117. Simon P, Gogotsi Y, Dunn B (2014) Materials science. Where do batteries end and supercapacitors begin? *Science* 343(6176):1210–1211

118. Lukatskaya MR, Mashtalir O, Ren CE et al (2013) Cation intercalation and high volumetric capacitance of two-dimensional titanium carbide. *Science* 341(6153):1502–1505
119. Hou RL, Liu B, Sun YL et al (2020) Recent advances in dual-carbon based electrochemical energy storage devices. *Nano Energy* 72:104728. <https://doi.org/10.1016/j.nanoen.2020.104728>
120. Xia Y, Mathis TS, Zhao MQ et al (2018) Thickness-independent capacitance of vertically aligned liquid-crystalline MXenes. *Nature* 557(7705):409–412
121. Jalili R, Aminorroaya-Yamini S, Benedetti TM et al (2016) Processable 2D materials beyond graphene: MoS₂ liquid crystals and fibres. *Nanoscale* 8(38):16862–16867
122. Kong J, Yang HC, Guo XZ et al (2020) High-mass-loading porous Ti₃C₂T_x films for ultrahigh-rate pseudocapacitors. *ACS Energy Lett* 5(7):2266–2274. <https://doi.org/10.1021/acsenergylett.0c00704>
123. Yu JL, Zhou J, Yao PP et al (2019) Antimonene engineered highly deformable freestanding electrode with extraordinarily improved energy storage performance. *Adv Energy Mater* 9(44):1902462. <https://doi.org/10.1002/aenm.201902462>
124. Li J, Yuan XT, Lin C et al (2017) Achieving high pseudocapacitance of 2D titanium carbide (MXene) by cation intercalation and surface modification. *Adv Energy Mater* 7(15):1602725. <https://doi.org/10.1002/aenm.201602725>
125. Guo QQ, Zhang XX, Zhao FY et al (2020) Protein-inspired self-healable Ti₃C₂ MXenes/rubber-based supramolecular elastomer for intelligent sensing. *ACS Nano* 14(3):2788–2797
126. Li Q, Wang YX, Wu YH et al (2019) Flexible cellulose nanofibrils as novel Pickering stabilizers: the emulsifying property and packing behavior. *Food Hydrocoll* 88:180–189. <https://doi.org/10.1016/j.foodhyd.2018.09.039>
127. Liu R, Ma LN, Niu GD et al (2017) Oxygen-deficient bismuth oxide/graphene of ultrahigh capacitance as advanced flexible anode for asymmetric supercapacitors. *Adv Funct Mater* 27(29):1701635. <https://doi.org/10.1002/adfm.201701635>
128. Zhu MS, Huang Y, Deng QH et al (2016) Highly flexible, freestanding supercapacitor electrode with enhanced performance obtained by hybridizing polypyrrole chains with MXene. *Adv Energy Mater* 6(21):1600969. <https://doi.org/10.1002/aenm.201600969>
129. VahidMohammadi A, Moncada J, Chen HZ et al (2018) Thick and freestanding MXene/PANI pseudocapacitive electrodes with ultrahigh specific capacitance. *J Mater Chem A* 6(44):22123–22133. <https://doi.org/10.1039/C8TA05807E>
130. Boota M, Gogotsi Y (2019) MXene-conducting polymer asymmetric pseudocapacitors. *Adv Energy Mater* 9(7):1802917. <https://doi.org/10.1002/aenm.201802917>
131. Couly C, Alhabeb M, Aken KLV et al (2017) Asymmetric flexible MXene-reduced graphene oxide micro-supercapacitor. *Adv Electron Mater* 4(1):1700339. <https://doi.org/10.1002/aelm.201700339>
132. Rosenman A, Markevich E, Salitra G et al (2015) Review on Li-sulfur battery systems: an integral perspective. *Adv Energy Mater* 5(16):1500212
133. Wei YJ, Tao YQ, Zhang CF et al (2016) Layered carbide-derived carbon with hierarchically porous structure for high rate lithium-sulfur batteries. *Electrochim Acta* 188:385–392. <https://doi.org/10.1016/j.electacta.2015.12.012>
134. Tang Q, Zhou Z, Shen PW (2012) Are MXenes promising anode materials for Li ion batteries? Computational studies on electronic properties and Li storage capability of Ti₃C₂ and Ti₃C₂X₂ (X = F, OH) monolayer. *J Am Chem Soc* 134(40):16909–16916
135. Yan BZ, Lu CJ, Zhang PG et al (2020) Oxygen/sulfur decorated 2D MXene V₂C for promising lithium ion battery anodes. *Mater Today Commun* 22:100713. <https://doi.org/10.1016/j.mtcomm.2019.100713>
136. Wei CL, Fei HF, Tian Y et al (2019) Room-temperature liquid metal confined in MXene paper as a flexible, freestanding, and binder-free anode for next-generation lithium-ion batteries. *Small* 15(46):e1903214
137. Chen C, Boota M, Xie XQ et al (2017) Charge transfer induced polymerization of EDOT confined between 2D titanium carbide layers. *J Mater Chem A* 5(11):5260–5265. <https://doi.org/10.1039/C7TA00149E>
138. Zhang D, Wang S, Li B et al (2019) Horizontal growth of lithium on parallelly aligned MXene layers towards dendrite-free metallic lithium anodes. *Adv Mater* 31(33):e1901820
139. Yu YX (2016) Prediction of mobility, enhanced storage capacity, and volume change during sodiation on interlayer-expanded functionalized Ti₃C₂ MXene anode materials for sodium-ion batteries. *J Phys Chem C* 120(10):5288–5296. <https://doi.org/10.1021/acs.jpcc.5b10366>
140. Zhao RZ, Qian Z, Liu ZY et al (2019) Molecular-level heterostructures assembled from layered black phosphorene and Ti₃C₂ MXene as superior anodes for high-performance sodium ion batteries. *Nano Energy* 65:104037. <https://doi.org/10.1016/j.nanoen.2019.104037>
141. Zhao MQ, Xie XQ, Ren CG et al (2017) Hollow MXene spheres and 3D macroporous MXene frameworks for Na-ion storage. *Adv Mater* 29(37):1702410. <https://doi.org/10.1002/adma.201702410>
142. Xie XQ, Zhao MQ, Anasori B et al (2016) Porous heterostructured MXene/carbon nanotube composite paper with high volumetric capacity for sodium-based energy storage devices. *Nano Energy* 26:513–523. <https://doi.org/10.1016/j.nanoen.2016.06.005>
143. Boota M, Anasori B, Voigt C et al (2016) Pseudocapacitive electrodes produced by oxidant-free polymerization of pyrrole between the layers of 2D titanium carbide (MXene). *Adv Mater* 28(7):1517–1522
144. Anasori B, Xie Y, Beidaghi M et al (2015) Two-dimensional, ordered, double transition metals carbides (MXenes). *ACS Nano* 9(10):9507–9516
145. Ma ZY, Zhou XF, Deng W et al (2018) 3D porous MXene (Ti₃C₂)/reduced graphene oxide hybrid films for advanced lithium storage. *ACS Appl Mater Interfaces* 10(4):3634–3643. <https://doi.org/10.1021/acsami.7b17386>
146. Ren CG, Zhao MQ, Makaryan T et al (2016) Porous two-dimensional transition metal carbide (MXene) flakes for high-performance Li-ion storage. *ChemElectroChem* 3(5):689–693. <https://doi.org/10.1002/celec.201600059>
147. Huang SQ, Dakhchoune M, Luo W et al (2018) Single-layer graphene membranes by crack-free transfer for gas mixture separation. *Nat Commun* 9(1):2632
148. Gao Q, Sun WW, Ilani-Kashkouli P et al (2020) Tracking ion intercalation into layered Ti₃C₂ MXene films across length scales. *Energy Environ Sci* 13(8):2549–2558. <https://doi.org/10.1039/D0EE01580F>
149. Ren CE, Hatzell KB, Alhabeb M et al (2015) Charge- and size-selective ion sieving through Ti₃C₂T_x MXene membranes. *J Phys Chem Lett* 6(20):4026–4031
150. Ding L, Li LB, Liu YC et al (2020) Effective ion sieving with Ti₃C₂T_x MXene membranes for production of drinking water from seawater. *Nat Sustain* 3(4):296–302
151. Xie XQ, Chen C, Zhang N et al (2019) Microstructure and surface control of MXene films for water purification. *Nat Sustain* 2(9):856–862
152. Chung DDL (2001) Electromagnetic interference shielding effectiveness of carbon materials. *Carbon* 39(2):279–285. [https://doi.org/10.1016/S0008-6223\(00\)00184-6](https://doi.org/10.1016/S0008-6223(00)00184-6)
153. Lee J, Jung KH, Choi Y et al (2020) Improved active interference canceling algorithms for real-time protection of 2nd/3rd level

- facilities in electronic warfare environment. *Appl Sci* 10(7):2405. <https://doi.org/10.3390/app10072405>
154. Hantanasirisakul K, Gogotsi Y (2018) Electronic and optical properties of 2D transition metal carbides and nitrides (MXenes). *Adv Mater* 30(52):e1804779
 155. Al-Saleh MH, Sundararaj U (2009) Electromagnetic interference shielding mechanisms of CNT/polymer composites. *Carbon* 47(7):1738–1746. <https://doi.org/10.1016/j.carbon.2009.02.030>
 156. Liu J, Zhang HB, Sun RH et al (2017) Hydrophobic, flexible, and lightweight MXene foams for high-performance electromagnetic-interference shielding. *Adv Mater* 29(38):1702367. <https://doi.org/10.1002/adma.201702367>
 157. Shahzad F, Alhabeib M, Hatter CB et al (2016) Electromagnetic interference shielding with 2D transition metal carbides (MXenes). *Science* 353(6304):1137–1140
 158. Song WL, Cao MS, Lu MM et al (2013) Alignment of graphene sheets in wax composites for electromagnetic interference shielding improvement. *Nanotechnology* 24(11):115708
 159. Yan DX, Pang H, Xu L et al (2014) Electromagnetic interference shielding of segregated polymer composite with an ultralow loading of *in situ* thermally reduced graphene oxide. *Nanotechnology* 25(14):145705
 160. Shahzad F, Kumar P, Kim YH et al (2016) Biomass-derived thermally annealed interconnected sulfur-doped graphene as a shield against electromagnetic interference. *ACS Appl Mater Interfaces* 8(14):9361–9369. <https://doi.org/10.1021/acsami.6b00418>
 161. Zeng ZH, Chen MJ, Jin H et al (2016) Thin and flexible multi-walled carbon nanotube/waterborne polyurethane composites with high-performance electromagnetic interference shielding. *Carbon* 96:768–777. <https://doi.org/10.1016/j.carbon.2015.10.004>
 162. Zhan YH, Wang J, Zhang KY et al (2018) Fabrication of a flexible electromagnetic interference shielding Fe_3O_4 @reduced graphene oxide/natural rubber composite with segregated network. *Chem Eng J* 344:184–193. <https://doi.org/10.1016/j.cej.2018.03.085>
 163. Lee SH, Kang D, Oh IK (2017) Multilayered graphene-carbon nanotube-iron oxide three-dimensional heterostructure for flexible electromagnetic interference shielding film. *Carbon* 111:248–257. <https://doi.org/10.1016/j.carbon.2016.10.003>
 164. Thomassin JM, Pagnouille C, Bednarz L et al (2008) Foams of polycaprolactone/MWNT nanocomposites for efficient EMI reduction. *J Mater Chem* 18(7):792–796. <https://doi.org/10.1039/B709864B>
 165. Liu L, Yang ZH, Deng CR et al (2012) High frequency properties of composite membrane with in-plane aligned Sendust flake prepared by infiltration method. *J Magn Magn Mater* 324(10):1786–1790. <https://doi.org/10.1016/j.jmmm.2011.12.038>
 166. Shen B, Zhai WT, Tao MM et al (2013) Lightweight, multifunctional polyetherimide/graphene@ Fe_3O_4 composite foams for shielding of electromagnetic pollution. *ACS Appl Mater Interfaces* 5(21):11383–11391
 167. Cao WT, Ma C, Tan S et al (2019) Ultrathin and flexible CNTs/MXene/cellulose nanofibrils composite paper for electromagnetic interference shielding. *Nano-Micro Lett* 11(1):1–17. <https://doi.org/10.1007/s40820-019-0304-y>
 168. Ma TY, Cao JL, Jaroniec M et al (2016) Interacting carbon nitride and titanium carbide nanosheets for high-performance oxygen evolution. *Angew Chem Int Ed Engl* 55(3):1138–1142
 169. Gao YY, Yan C, Huang HC et al (2020) Microchannel-confined MXene based flexible piezoresistive multifunctional micro-force sensor. *Adv Funct Mater* 30(11):1909603. <https://doi.org/10.1002/adfm.201909603>
 170. Huang K, Li Z, Lin J et al (2018) Two-dimensional transition metal carbides and nitrides (MXenes) for biomedical applications. *Chem Soc Rev* 47(14):5109–5124
 171. Rasool K, Helal M, Ali A et al (2016) Antibacterial activity of $\text{Ti}_3\text{C}_2\text{T}_x$ MXene. *ACS Nano* 10(3):3674–3684
 172. Jastrzębska AM, Karwowska E, Wojciechowski T et al (2019) The atomic structure of Ti_2C and Ti_3C_2 MXenes is responsible for their antibacterial activity toward *E. coli* bacteria. *J Mater Eng Perform* 28(3):1272–1277. <https://doi.org/10.1007/s11665-018-3223-z>
 173. Li RY, Zhang LB, Shi L et al (2017) MXene Ti_3C_2 : an effective 2D light-to-heat conversion material. *ACS Nano* 11(4):3752–3759. <https://doi.org/10.1021/acsnano.6b08415>
 174. Zhao JQ, Yang YW, Yang CH et al (2018) A hydrophobic surface enabled salt-blocking 2D Ti_3C_2 MXene membrane for efficient and stable solar desalination. *J Mater Chem A* 6(33):16196–16204. <https://doi.org/10.1039/c8ta05569f>
 175. Zhang Q, Yi G, Fu Z et al (2019) Vertically aligned *Janus* MXene-based aerogels for solar desalination with high efficiency and salt resistance. *ACS Nano* 13(11):13196–13207
 176. An H, Habib T, Shah S et al (2018) Surface-agnostic highly stretchable and bendable conductive MXene multilayers. *Sci Adv* 4(3):eaq0118
 177. Li FuXY, Chen S et al (2020) Hydrophobic and stable MXene-polymer pressure sensors for wearable electronics. *ACS Appl Mater Interfaces* 12(13):15362–15369
 178. Cheng YF, Ma YN, Li LY et al (2020) Bioinspired microspines for a high-performance spray $\text{Ti}_3\text{C}_2\text{T}_x$ MXene-based piezoresistive sensor. *ACS Nano* 14(2):2145–2155
 179. Kim SJ, Koh HJ, Ren CE et al (2018) Metallic $\text{Ti}_3\text{C}_2\text{T}_x$ MXene gas sensors with ultrahigh signal-to-noise ratio. *ACS Nano* 12(2):986–993
 180. Chen WY, Lai SN, Yen CC et al (2020) Surface functionalization of $\text{Ti}_3\text{C}_2\text{T}_x$ MXene with highly reliable superhydrophobic protection for volatile organic compounds sensing. *ACS Nano* 14(9):11490–11501. <https://doi.org/10.1021/acsnano.0c03896>
 181. Shuck CE, Gogotsi Y (2020) Taking MXenes from the lab to commercial products. *Chem Eng J* 401:125786. <https://doi.org/10.1016/j.cej.2020.125786>



Lu Shao is a tenure-track Professor in School of Chemistry and Chemical Engineering at Harbin Institute of Technology (HIT). He received his Ph.D. (2005) from National University of Singapore. He is elected as a Fellow of the Royal Society of Chemistry (FRSC, UK) in 2020. His research interests are membrane separation and synthesis/fabrication of advanced functional material towards environmental remediation and energy harvesting such as carbon capture, water treatment and hydrogen purification. He serves as Editorial Board Member of *Journal of Membrane Science*, Editorial Advisory Board Member of *ACS ES&T Engineering*, and Associate Editor of *Advanced Composites & Hybrid Materials*.